Journal of Nanobiotechnology

RESEARCH

Open Access

Exploring the cytotoxic and antioxidant properties of lanthanide-doped ZnO nanoparticles: a study with machine learning interpretation

Jorge L. Mejia-Mendez[1], Edwin E. Reza-Zaldívar[2], A. Sanchez-Martinez[3], O. Ceballos-Sanchez[3], Diego E. Navarro-López[4], L. Marcelo Lozano[4], Juan Armendariz-Borunda[5,6], Naveen Tiwari[7*], Daniel A. Jacobo-Velázquez[2,4*], Gildardo Sanchez-Ante[4*] and Edgar R. López-Mena[4*]

Abstract

Background Lanthanide-based nanomaterials offer a promising alternative for cancer therapy because of their selectivity and effectiveness, which can be modified and predicted by leveraging the improved accuracy and enhanced decision-making of machine learning (ML) modeling.

Methods In this study, erbium (Er^{3+}) and ytterbium (Yb^{3+}) were used to dope zinc oxide (ZnO) nanoparticles (NPs). Various characterization techniques and biological assays were employed to investigate the physicochemical and optical properties of the (Er, Yb)-doped ZnO NPs, revealing the influence of the lanthanide elements.

Results The (Er, Yb)-doped ZnO NPs exhibited laminar-type morphologies, negative surface charges, and optical bandgaps that vary with the presence of Er^{3+} and Yb^{3+}. The incorporation of lanthanide ions reduced the cytotoxicity activity of ZnO against HEPG-2, CACO-2, and U87 cell lines. Conversely, doping with Er^{3+} and Yb^{3+} enhanced the antioxidant activity of the ZnO against DPPH, ABTS, and H_2O_2 radicals. The extra tree (ET) and random forest (RF) models predicted the relevance of the characterization results vis-à-vis the cytotoxic properties of the synthesized NPs.

Conclusion This study demonstrates, for the first time, the synthesis of ZnO NPs doped with Er and Yb via a solution polymerization route. According to characterization results, it was unveiled that the effect of optical bandgap variations influenced the cytotoxic performance of the developed lanthanide-doped ZnO NPs, being the undoped ZnO NPs the most cytotoxic ones. The presence alone or in combination of Er and Yb enhanced their scavenging

*Correspondence:
Naveen Tiwari
naveen.tiwari@usc.es
Daniel A. Jacobo-Velázquez
djacobov@tec.mx
Gildardo Sanchez-Ante
gildardo.sanchez@tec.mx
Edgar R. López-Mena
edgarl@tec.mx

Full list of author information is available at the end of the article

capacity. ML models such as ET and RF efficiently demonstrated that the concentration and cell line type are key parameters that influence the cytotoxicity of (Er, Yb)-doped ZnO NPs achieving high accuracy rates of 98.96% and 98.67%, respectively. This study expands the knowledge of lanthanides as dopants of nanomaterials for biological and medical applications and supports their potential in cancer therapy by integrating robust ML approaches.

Graphical abstract

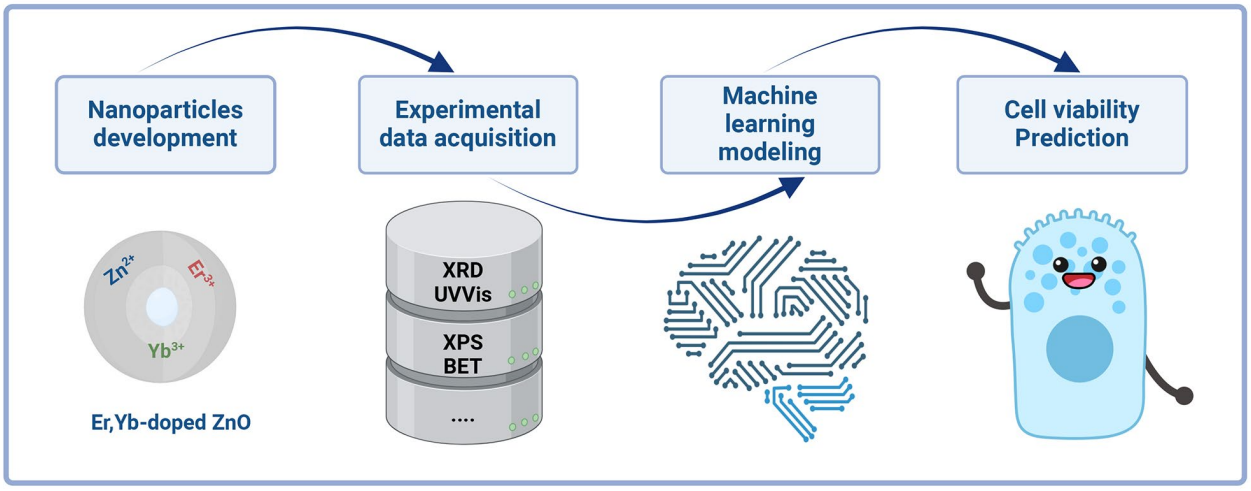

Keywords Rare-earth elements, Optical bandgap, Nanocytotoxicity, Antioxidant activity, Machine learning

Background

Cancer is a leading cause of high morbidity and mortality rates worldwide. According to the Global Cancer Observatory, the cancers with the highest global incidence are associated with lung (12.4%), breast (11.5%), colorectum (9.6%), prostate (7.3%), and liver (4.3%) cancer [1, 2]. Gliomas are also highly prevalent in countries such as the United States of America, France, Korea, and Denmark [3]. Various risk factors contribute to cancer development, including elevated free radical levels [4, 5]. Both natural and synthetic antioxidants can inhibit free radical formation within biological systems via different mechanisms [6, 7]. However, compared to natural sources, synthetic antioxidants, such as nanomaterials (NMs), offer high stability and can regulate key molecular and cellular processes by preventing or interfering with free radical formation [8]. Synthetic antioxidants can be derived from various raw materials, including metal oxides and lanthanides [9].

Lanthanides, also known as rare-earth elements, are a series of chemically and biologically active metals with applications in immune therapy [10], bioimaging, temperature sensing [11], photodynamic therapy [12], and the development of antibacterial agents [13]. Unlike other materials, lanthanide-based NMs are advantageous due to their affordability, ease of manipulation through various synthesis routes [14, 15], intrinsic physicochemical properties derived from the shielding effect of 4*f* electrons, and enhanced magnetic and optical properties. Upconversion nanoparticles (UPNPs) are inorganic matrices doped with lanthanide cations that can be excited using low-energy near-infrared light. The most studied systems are $NaYF_4$: Er^{3+}, Yb^{3+}, wherein erbium (Er^{3+}) serves as an activator and ytterbium (Yb^{3+}) as a sensitizer. This system requires excitation by a 980-nm light source. This system exhibited cytotoxicity against A549 cells and in murine models of Lewis lung carcinoma tumors, reducing cell viability at concentrations of 100–400 µg/mL and inhibiting tumor growth 24 h after injection [16]. In nanomedicine, Er^{3+} has been used to synthesize nanoparticles (NPs) with activity against diabetes and postprandial hyperglycemia models [17]. Er^{3+}-doped NPs have also been used to coat poly(ethylene) oxide nanofibers, exhibiting low cytotoxicity toward MCF-7 cells and enhanced contrast in magnetic resonance imaging [18]. Other studies have demonstrated that Er-based NPs are suitable for biomedical applications because of they prevent aberrations in reactive oxygen species (ROS) levels, genetic material integrity, or apoptotic gene expression in human skin fibroblast cells [19]. Ytterbium (Yb^{3+}) has also been used to develop NPs with anti-inflammatory properties, anticancer activity against breast cancer cell lines, and antibacterial effects against *Escherichia coli (E. coli)* and *Staphylococcus aureus* [20]. Upon combining with other rare-earth elements such as cerium oxide, Yb-based NPs exhibit

cytotoxicity against colon cancer cell lines (HCT-116) and antimicrobial properties against *E. coli* and *Candida albicans* [21]. Furthermore, nanocomposites of Yb_2O_3 and graphene oxide have been developed as a biocompatible material for bone replacement applications, facilitating osteoblast cell attachment and proliferation [22].

Zinc is a transitional metal characterized by its high density, low melting point, and capacity to form various oxidation states. Zinc has been utilized as a dopant for nanobiotechnological applications, especially in cadmium oxide nanorods for antimicrobial applications [23, 24] and copper oxide NPs for crop yield protection [23]. Zinc oxide (ZnO) is the oxide form of zinc. It is a versatile powdery solid metal oxide widely used in the synthesis of nanostructures owing to its intrinsic properties, photocatalytic activity, and high ultraviolet (UV) absorption capacity [24]. In nanobiotechnology, ZnO is an ideal material for synthesizing nanostructures with distinct structural arrangements, physicochemical features, biological activities [27], and the capacity to degrade dyes such as rhodamine B [25]. ZnO NPs have been doped with various materials to enhance their therapeutic performance for both in vitro and in vivo applications. For instance, ZnO NPs doped with gold or palladium exhibit considerable antibacterial activity at low concentrations [26]. Conversely, ZnO NPs doped with lanthanides such as cerium, neodymium, erbium, thulium, and ytterbium serve as versatile probes for magnetic resonance and computed tomography imaging and as effective agents for chemotherapy, radiotherapy, and photodynamic therapy in leukemia models [27, 28].

Recently, machine learning (ML) has become a powerful tool in efficient designing and screening NMs based on their electronic, thermal, optical, and biological properties [29, 30]. In nanobiotechnology, ML models, such as multiple linear regression models, Monte Carlo simulations, and linear discriminant analysis, use response and independent variables, probability distributions, and descriptors to understand and predict NMs' effects in vitro and in vivo [31]. ML has also been applied to study the anticancer and antioxidant activities, as well as the in vivo toxicity of ZnO NPs doped with La^{3+} and Sm^{3+} [32]. Recently, deep learning models have been used to determine feature importance, providing deeper insights into the modeled processes [33, 34].

This study systematically analyzes the effects of doping ZnO with Er^{3+} and Yb^{3+} on its structural, morphological, optical, and compositional properties. The nanocytotoxicity of these materials against various cancer cell lines associated with major global cancers, and their antioxidant activity was studied using 2,2-diphenyl-1-picrylhydrazyl (DPPH), 2,2′-azino-bis(3-ethylbenzothiazoline-6-sulfonic acid (ABTS), and H_2O_2 radicals. The generated data were integrated into a dataset and analyzed using ML models. A methodology based on Shapley indices was applied to determine attribute importance, identifying the NP characteristics most relevant to their nanocytotoxicity. Results revealed that (Er, Yb)-doped ZnO NPs exhibited mesoporous features and laminar-type morphologies, with distinct performance against hepatocellular, colon, and glioma cancer cells, and possess different capacities to scavenge free radicals when used within the concentration range of 5–250 µg/mL. Of the trained models, the extra tree (EXT) and decision tree (DT) models efficiently predicted the developed materials' nanocytotoxicity with an accuracy rate of 98.96% and 98.67%, respectively. To the best of our knowledge, this study is the first to demonstrate the effect of variations in optical bandgaps in lanthanide-doped ZnO NPs on nanocytotoxicity. It also highlights the importance of ML modeling in understanding nanostructures with biological and medical applications. Scheme 1 depicts the workflow of this study.

Materials and methods

Synthesis of NMs

Undoped and (Er, Yb)-doped ZnO nanoparticles were synthesized using a solution-polymerization method. 0.2 g of polyvinyl alcohol (PVA, Mw: 30000–70000) was dissolved in 100 mL of deionized water while stirring at 80℃ until complete dissolution. Upon obtaining a transparent solution, stoichiometric amounts of zinc, erbium, and ytterbium precursors (i.e., $Zn(NO_3)_2.6H_20$, $Er(NO_3)_3.5H_2O$, and $Yb(NO_3)_3.5H_2O$, respectively) were incorporated to obtain $Zn_{1-x}(Er, Yb)_xO$ solutions. The solutions were stirred at 80℃ until all water evaporated. The resulting precursor powders were then dried at 200℃ for 4 h, and then calcined at 450℃ for 3 h in the air. Figure 1a depicts the synthesis process. The samples were labeled Z, ZE, ZEY, or ZY based on the presence of Er^{3+} or Yb $^{3+}$. These mean, undoped ZnO (Z), 10 at% of Er^{3+}-doped ZnO (ZE), 5 at% of Er^3+5 at% of Yb^3-doped ZnO (ZEY), and 10 at% of Yb^{3+}-doped ZnO (ZY).

Characterization of the NMs

The crystal structures of the NPs were characterized via X-ray diffraction (XRD) using an Empyrean diffractometer (PANalytical) equipped with a copper anode (λ=1.5406 Å). The XRD patterns were obtained for 2θ ranging from a 20° to 70° with a step size of 0.01°. Morphology of the NPs was investigated via field emission scanning electron microscopy (FESEM) (TESCAN MIRA3 model). Transmission electron microscopy (TEM)/high-resolution transmission electron microscopy (HRTEM)/scanning transmission electron microscopy (STEM) analyses were conducted using an FEI-Titan microscope operating at 300 kV. Energy-dispersive spectroscopy (EDS) was conducted to identify the

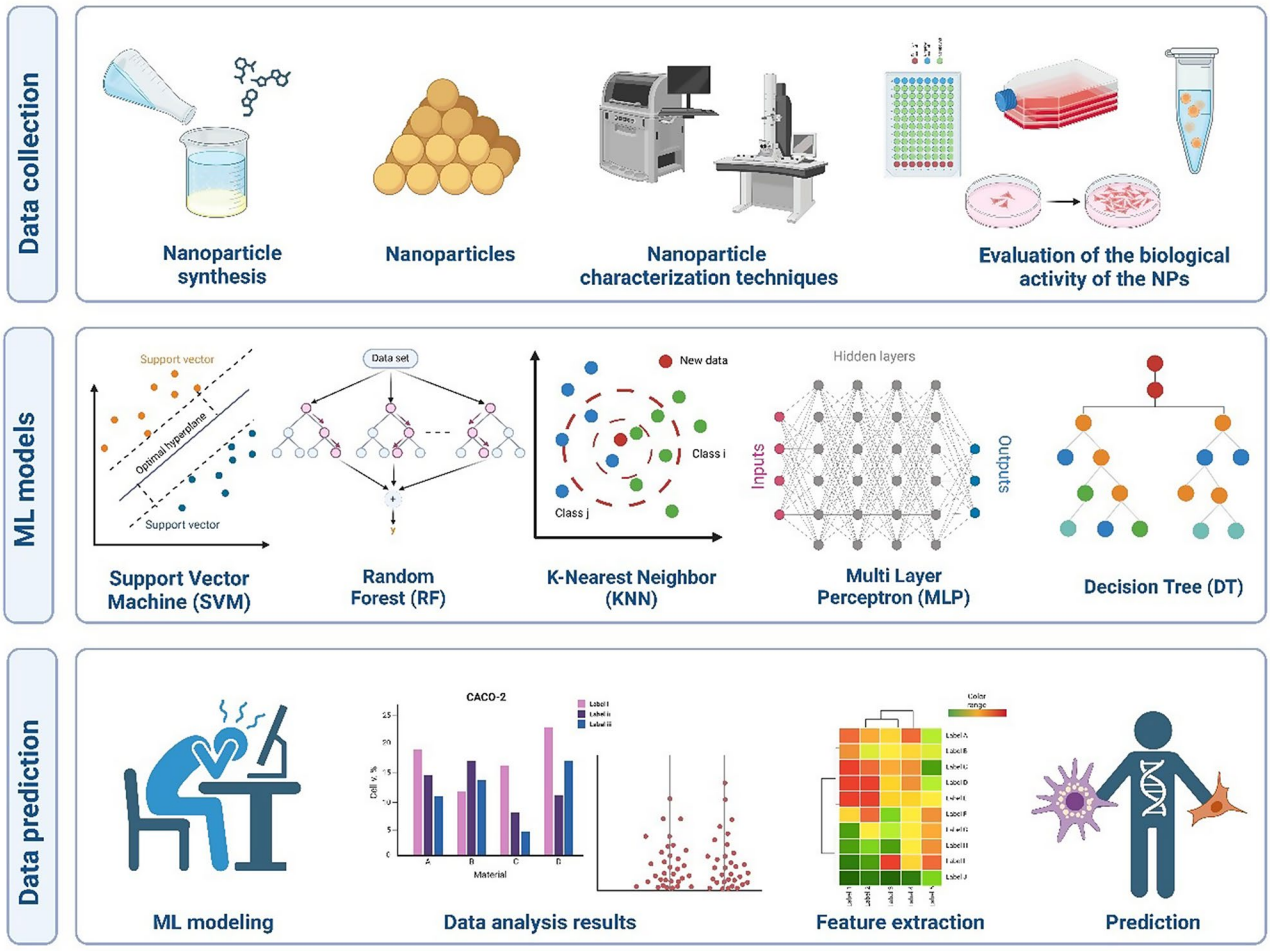

Scheme 1 Design and workflow for the synthesis and physicochemical characterization of (Er, Yb)-doped ZnO nanoparticles (NPs), demonstrating the advantages of incorporating machine learning (ML) models to predict their cytotoxicity

elements in the sample selected area electron diffraction (SAED) was used for further analysis. The Brunauer–Emmett–Teller (BET) method was used to determine the specific surface area (SBET) by employing a Bel-Japan MiniSorp II instrument. The optical properties were assessed using absorption spectra obtained with a Cary-5000 UV–visible (UV–Vis, Agilent Technologies) spectrometer equipped with a polytetrafluoroethylene integration sphere. HR X-ray photoelectron spectroscopy (HR-XPS) (Thermo Scientific, K-Alpha) was performed using a monochromatic Al K_α source (hυ = 1486.7 eV). The HR-XPS spectra of Zn 2p, O 1s, C 1s, Er 4d, and Yb 4d core levels were collected at a pass energy of 15 eV. All spectra were aligned to the C 1s signal at 284.8 eV, which is primarily associated with adventitious carbon. The takeoff angle of the photoelectron was set to 0° relative to the normal of the sample surface and the axis of the hemispherical analyzer's input lens. The spectra were deconvoluted using AAnalyzer® software, which includes essential features for active background subtraction and spherical wavelet signal correction (SVSC) background adjustment for accurate XPS analysis [35].

Evaluation of biological activities

Cytotoxic activity

The cytotoxicities of Z, ZE, ZEY, and ZY were assessed using the 3–4,5-dimethylthiazol-2-yl]-2,5-diphenyl-tetrazolium bromide (MTT) assay in HEPG-2 (ATCC HB-8065), RAW 264.7 (ATCC TIB-71), CACO-2 (ATCC HTB-37), and U87 (ATCC HTB-14) cell lines. Cell lines were cultured in Dulbecco's Modified Eagle Medium F-12 containing 10% fetal bovine serum in a humidified atmosphere at 37℃ under 5% CO_2. For the MTT assay, 15,000 cells were seeded into each well of a 96-well plate and incubated under these conditions. The following day, the medium was replaced with fresh medium, following which Z, ZE, ZEY, and ZY were added at concentrations of 5, 20, 50, 100, and 250 µg/mL, respectively. The plate was then incubated for 24 h at 37℃ under 5% CO_2. After incubation, 25 µL of the MTT working solution (5 mg/mL) was added to each well. The resulting formazan

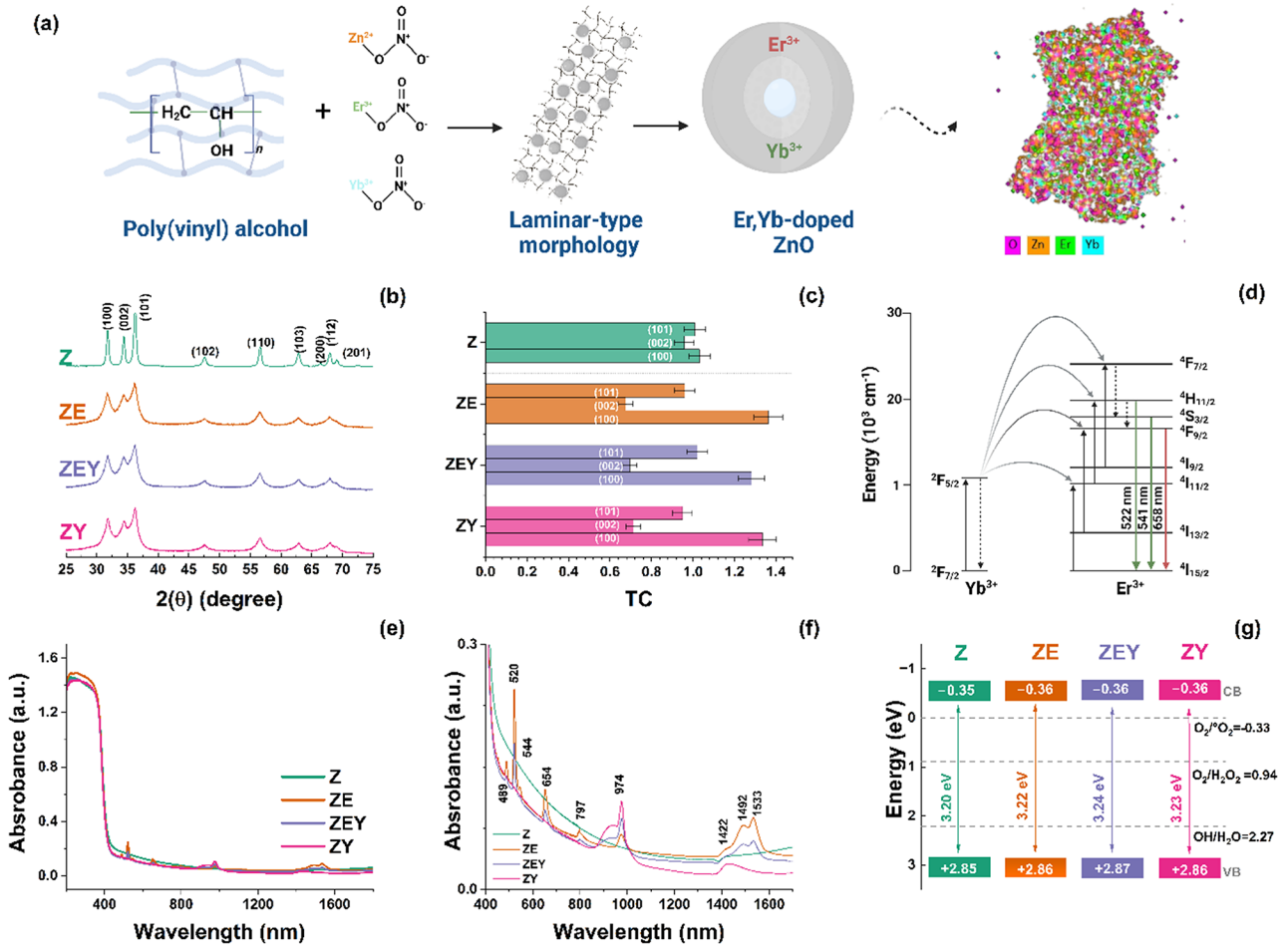

Fig. 1 (**a**) Synthesis process, (**b**) X-ray diffraction (XRD) patterns, (**c**) texture coefficient (TC), (**d**) Er^{3+}/Yb^{3+} energy level diagram, (**e**) absorbance spectra, (**f**) magnified absorbance spectra in the range of 400–1600 nm, and (**g**) optical bandgap, conduction band (CB), and valence band (VB) values of the (Yb, Er)-doped ZnO NPs

crystals were solubilized with technical grade dimethylsulfoxide, and absorbance was measured at 490 nm using a Synergy HTX Multi-Mode Microplate Reader (BioTek). The experiments were performed in triplicate.

Antioxidant activity

The antioxidant activities of Z, ZE, ZEY, and ZY was assessed using DPPH, ABTS, and H_2O_2 assays. For the DPPH assay, 4 mg of DPPH was dissolved in 100 mL of technical grade ethanol and moderately stirred in the dark for 2 h. Then, 200 µL of this solution was mixed with 20 µL of (Er, Yb)-doped ZnO NPs at concentrations of 5, 20, 50, 100, and 250 µg/mL. The absorbance was recorded at 517 nm using a Cary-5000 UV–Vis spectrophotometer (Agilent Technologies). For the ABTS assay, 19.7 mg of ABTS powder was dissolved in 50 mL of distilled water and mixed with 186.2 mg of $K_2S_2O_8$ for 1 h in the dark. Next, 200 µL of the ABTS solution was mixed with 20 µL of various concentrations of (Er, Yb)-doped ZnO NPs (5, 20, 50, 100, and 250 µg/mL). After 6 min of incubation, absorbance was determined at 734 nm using the same spectrophotometer. For the H_2O_2 assay, 70 µL of a 40 mmol L^{-1} H_2O_2 solution was mixed with 100 µL of (Er, Yb)-doped ZnO NPs at various concentrations and incubated in the dark for 30 min. The absorbance was measured at 230 nm using the same spectrophotometer. Ascorbic acid was used as a positive control in all the three antioxidant assays despite the differences in experimental procedures.

Statistical analysis

The experimental data were analyzed by ANOVA with a post-hoc Tukey HSD test with a 95% confidence. Statistical significance was marked with asterisks depending on the p-value: $^{*}p \leq 0.05$, $^{**}p \leq 0.01$, $^{***}p \leq 0.001$.

ML modeling

Dataset

The original dataset contained 480 observations with 22 attributes and a response variable, CellVia (cell viability

percentage). The attributes included the NP concentrations used in the biological assays (conc), optical band gap (BG), zinc content (Zn), average crystallite size (CS), valence band (VB), conduction band (VB), etc. The dataset contained categorical attributes, such as the material type (four categories) and cell type (four categories).

Preprocessing

Categorical variables were handled using One Hot Encoding, expanding the dataset to 28 attributes. Data normalization was performed to scale the input vectors to unit norms. The dataset was then divided into a training set (70%, 336 observations) and a validation set (30%, 144 observations).

Experiments

Eight models were trained: linear regression (LR), random forest (RF), extremely random trees (EXT), decision tree (DT), multilayer perceptron (MLP), k-nearest neighbor (KNN), gradient boost (GB), and support vector machine (SVR). Default parameters were used for all models except the MLP, which was set to a maximum of 50,000 epochs. Cross-validation was employed for the model selection to address potential bias due to the split in the initial training validation data and the relatively small dataset size.

K-fold cross-validation method was performed by dividing the dataset into k disjoint subsets. One subset was kept "hidden" for validation, and the model was trained on the remaining k−1 subsets. This process was iterated k times with performance metrics averaged across iterations to facilitate fair model performance comparison.

After identifying the best performing model, we analyzed the attribute importance using the Shapley indices, which is originally proposed for measuring players' power in a voting game. This method, adapted into the Shapley additive explanations (SHAP) technique [36], quantifies each attribute's contribution to the prediction. SHAP is increasingly important in the field of explainable artificial intelligence to provide insights into model decision-making.

Table 1 Geometrical parameters of undoped and doped ZnO nanoparticles (NPs)

Material	Lattice parameter (Å)		V_{cell} (Å)	D (nm) ± 5%
	a	c		
Z	3.251	5.209	4.769	18
ZE	3.255	5.201	4.780	17
ZEY	3.248	5.213	4.765	12
ZY	3.283	5.204	4.857	13

Results and discussion

Material characterization

The effects of incorporation of Er^{3+} and Yb^{3+} in the crystal structure of ZnO (Fig. 1a) was analyzed via XRD, with the results shown in Fig. 1b. All samples matched the (100), (002), (101), (102), (110), (103), (200), (112), and (201) planes, corresponding to the hexagonal wurtzite structure of ZnO (JCPDS# 36-1451). Incorporation of the lanthanide elements reduced the crystallinity of ZnO, although no secondary phases related to the doping elements were observed. A slight shift in 2θ position and a decrease in average crystallite size were also observed. Various geometrical parameters, such as lattice parameters, average crystallite size, and unit cell volume were calculated from the XRD analysis, with the results presented in Table 1. Incorporating rare earth dopant ions into the ZnO matrix induces structural changes such as crystal lattice deformations and the appearance of structural defects, e.g., oxygen and Zn vacancies. Incorporating rare earth ions promotes the deformation of the ZnO crystal lattice, making the diffraction peaks broader and less intense compared with undoped ZnO nanoparticles. This occurs because the ionic radius values of Yb^{3+} (0.86 Å), Er^{3+} (0.89 Å), and Zn^{2+} (0.74 Å) differ [37]. The changes in the crystal lattice promote the formation of internal strain and structural defects, leading to changes in the grain boundaries. Meanwhile, it is well known that the preferential orientation planes largely determine the physicochemical properties of ZnO nanoparticles. ZnO is a polar crystal since it is composed of tetrahedrally coordinated O^{2-} and Zn^{2+} ions in alternating planes along the c-axis. The lattice parameters a and c are related to the (101) and (002) planes, respectively. Increasing the doping level prevents grain growth in the (002) direction, as observed in Fig. 1c. In addition, (001) and (002) are polar planes, whereas (100) and (101) are non-polar planes. The polar planes are related to reactive oxygen species (ROS) formation. A major proportion of polar faces in ROS production can be observed [38].

Figure 1d depicts an energy level diagram of Er^{3+}–Yb^{3+} to understand the mechanism of the UC (upconversion) process. The energy transfer from Yb^{3+} to Er^{3+} ions and the nonradiative relaxation (NR) from excited Er^{3+} are involved In the Er^{3+}-Yb^{3+} up-conversion process and play an important role in populating the high-energy states of Er^{3+} [39]. Hence, the Yb^{3+} ions are used as active ions (or sensitizers for the Er^{3+} ions) due to the high absorption at approximately 977 nm, since beneficial energy transfer occurs between the Yb^{3+} ions and Er^{3+} ions. The high absorption cross-section of the Yb^{3+} ions at ~975 nm allows them to capture NIR photons efficiently. After absorbing the NIR photons, the Yb^{3+} ions transfer their energy non-radiatively to nearby Er^{3+} ions. This energy transfer process excites the Er^{3+} ions from their ground

state of $^4I_{15/2}$ to higher energy levels as $^4I_{11/2}$. This allows the up-conversion process between Er^{3+} ions and ZnO, which can be described in several steps [40]: (i) In the excitation step, the Er^{3+} ions are excited from the ground state $^4I_{15/2}$ to the higher energy level $^4I_{11/2}$ by absorbing photons. (ii) During energy transfer up-conversion, two types of energy transfer mechanisms are necessary. The first involves the energy transfer from an excited Er^{3+} ion to a neighboring Er^{3+} ion, leading to excitation to higher levels, such as $^4F_{7/2}$ or $^4S_{3/2}$; the second is excited state absorption, where an already excited Er^{3+} ion absorbs another photon and is excited to higher states. (iii) In the emission step, after reaching the higher energy levels, the Er^{3+} ions relax back to their ground state, emitting photons in the visible range. The typical emission transitions are $^2H_{11/2} \rightarrow {}^4I_{15/2}$ (green emission), $^4S_{3/2} \rightarrow {}^4I_{5/2}$ (green emission), and $^4F_{9/2} \rightarrow {}^4I_{15/2}$ (red emission).

Figure 1e shows the absorbance spectra of the lanthanide-doped and undoped ZnO NPs in the range of 200–1800 nm. All samples exhibited an absorption edge at near 380 nm, corresponding to the direct bandgap of ZnO [41]. Figure 1f shows a magnified view of the absorbance spectra between 400 and 1800 nm, revealing several absorption bands corresponding to the optical transitions of Er^{3+} and Yb^{3+}. The six absorption peaks observed in ZE nanoparticles correspond to specific transitions of Er^{3+} ions from their ground state $^4I_{15/2}$ to higher energy levels. All these peaks are significant because they indicate the energy levels involved in the up-conversion process. The optical transition of $^4I_{15/2} \rightarrow {}^4I_{11/2}$ corresponds to an absorption peak in the NIR region (~974 nm). This is a primary transition involved in the initial excitation of Er^{3+} ions. $^4I_{15/2} \rightarrow {}^4I_{9/2}$ is related to the NIR absorption peak (~797 nm). The $^4I_{15/2} \rightarrow {}^4F_{9/2}$ transition leads to an absorption peak in the visible region (~654 nm). The $^4I_{15/2} \rightarrow {}^4S_{3/2}$ (~544 nm) and $^4I_{15/2} \rightarrow {}^2H_{11/2}$ (~520 nm) transitions correspond to green absorption peaks. Finally, the $^4I_{15/2} \rightarrow {}^4G_{11/2}$ transition is related to the near-ultraviolet region peak (~380 nm) [42]. The optical bandgap was calculated from the absorbance spectra using the Kubelka–Munk function [43]:

$$F(R_\infty) = \frac{(1 - R_\infty)^2}{2R_\infty} \quad (1)$$

where R_∞ is the absolute reflectance, calculated by the $R_{\text{sample}}/R_{\text{spectralon}}$ ratio. In addition, the energies of the conduction band and valence band were evaluated, and the results are shown in Fig. 1g. The calculated bandgap values for Z, ZE, ZEY, and ZY were 3.20, 3.22, 3.24, and 3.23 eV, respectively.

Figure 2 shows typical scanning electron microscopy (SEM) images of (Er, Yb)-doped ZnO NPs. PVA was used as a stabilizing agent to control the shape of the NPs. Initially, low-magnification images (Fig. 2a) of Z and ZY are shown, providing an overview of the microstructure. The fuel releases gases during combustion, resulting in a foamy microstructure. PVA is also known to form "materials sheets," as observed in [44]. Subsequently, high-magnification images (Fig. 2b) of all samples are shown, revealing a fully nanostructured sheet-surface. The average grain sizes calculated from these images were 30 nm for Z, 34 nm for ZE, 31 nm for ZEY, and 32 for ZY, with a standard deviation or error margin of ±5% (Fig. 2c). Statistical analysis indicated notable differences in the grain size (p-value < 0.05) between samples Z and ZE. No significant difference in the grain size compared with Z was observed when both ZEY double doping and ytterbium doping were applied to the material. However, Er^{3+} caused modifications (p-value < 0.5) in the grain size.

Figure 2d shows the specific surface area and pore volume distribution results, analyzed using the BET method. For Z, ZE, ZEY, and ZY, the respective SBET values were 10.12, 26.85, 34.29, and 35.20 m^2/g and the respective pore diameters were 18.51, 35.14, 35.44, and 36.80 Å. The molecular weight of doped nanoparticles increases according to the doping type; when more precursor nitrate salt is needed, more gases are consequently liberated and greater porosity forms during the synthesis process. All the samples were mesoporous, exhibiting type IV N_2 adsorption-desorption isotherms with a type H3 hysteresis loop [45]. Figure 2e shows the hydrodynamic diameter of the NPs, which are approximately 661, 884, 4683, and 1657 nm for Z, ZE, ZEY, and ZY, respectively. The hydrodynamic diameters were higher than those reported via XRD or SEM, indicating NP agglomeration in aqueous media. The zeta potential (ζ) values for Z, ZE, ZEY, and ZY were −37.4, −7.9, −17.4, and −5.2 mV, respectively (see Fig. 2f). The variation in the zeta potential (ζ potential) value after doping was due to alterations in the surface charge distribution and electrostatic interactions [46]. Doping introduces foreign atoms into the ZnO lattice, which can affect the surface charge by changing the balance of positive and negative charges on the particle surface. Furthermore, this affects the ionization state and the adsorption of ions or molecules from the surrounding medium, thereby affecting the overall zeta potential. The zeta potential values for all the samples were between −30 and 30 mV, indicating stable suspension. However, the ZY sample's zeta potential was near 0, potentially due to the electronic configuration of Yb^{3+} (the ionic radius was also small compared with Er^{3+}). This affects the surface charge of ZnO, where two phenomena can happen: the neutralization of more surface charges or the creation of a different surface state that results in a lower zeta potential [47].

TEM was employed to analyze these NPs in more detail compared with the FESEM image analysis (Fig. 3a).

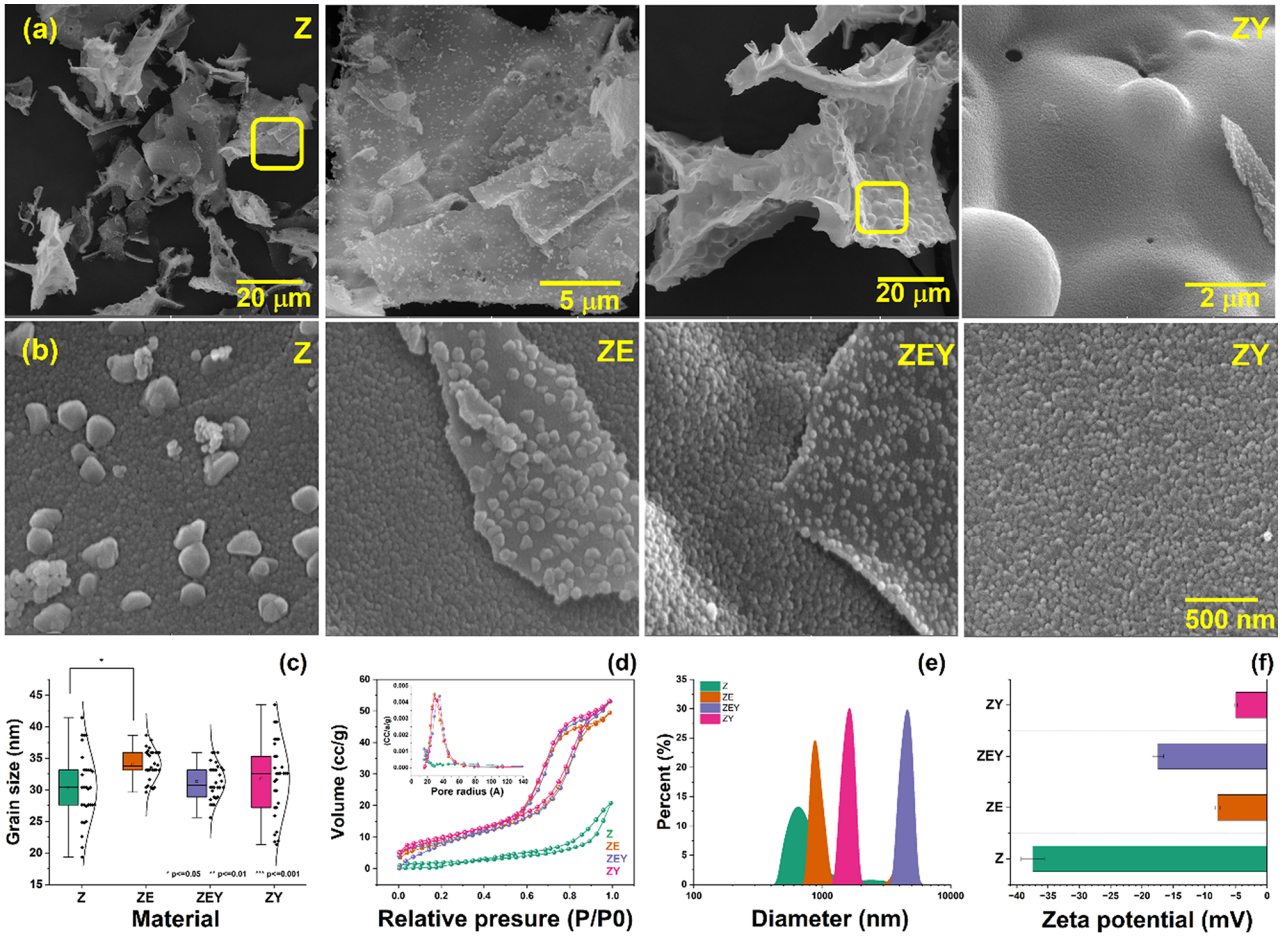

Fig. 2 (**a**) Low- and (**b**) high-magnification scanning electron microscopy (SEM) images of the as-prepared (Er, Yb)-doped ZnO NPs. (**c**) Grain size distribution and (**d**) N_2 adsorption–desorption isotherm plots (inset: pore size distribution) of the NPs. (**e**) Size distribution analysis of dynamic light scattering (DLS). (**f**) Zeta potentials (ζ) of Z, ZE, ZEY, and ZY

A TEM image of the ZEY NPs, shown in Fig. 3b, depicts a section of the sheet where the NPs are interconnected, with the average grain size calculated to be 15 nm±5%. The difference in the grain size values between the SEM and TEM analyses could be attributed to the different spatial resolutions of the SEM (low) and TEM (high) techniques. SEM images provide information about the surface morphology, while TEM images give in-depth information about the nanoparticles. Hence, SEM can obtain a higher grain size compared with TEM results. The image analysis was performed using ImageJ software and the thresholding procedure [48]. Figure 3c shows an HRTEM image of the ZEY NPs. Analyzing the high-resolution TEM micrograph allowed the interplanar distance (d) to be estimated by applying the inverse fast Fourier transform. The obtained values were compared with PDF card No. 36-1451 in Jade software, and the corresponding diffraction plane was identified. The interplanar distance of 2.80 Å was consistent with the diffraction plane (100), while that of 2.59 Å was associated with the diffraction plane (002). Both the interplanar distance values were consistent with the preferential orientation planes observed in the diffraction pattern in Fig. 1b. In the SAED pattern (Fig. 3d), a single-phase material will show a consistent and uniform diffraction pattern corresponding to one crystal structure, whereas a multiphase material will show additional diffraction spots or rings, indicating the presence of other crystalline phases. The SAED pattern can also display changes due to doping, such as slight shifts in the diffraction peaks or changes in the intensity. Analyses of the SAED pattern with ImageJ software revealed that the rings corresponded to the diffraction planes observed in the XRD results, where no secondary phases were observed. Figure 3e shows the Energy-dispersive X-ray spectroscopy (EDS) mapping of the ZEY NPs.

The elements and chemical states on the surface of ZnO and (Er, Yb)-doped ZnO were investigated via XPS, as shown in Fig. 4. The spectra were simultaneously fitted to ensure a robust fit for the experimental data. Figure 4a depicts the Zn 2p spectra with a spin–orbit separation of 23.10 eV. To fit the Zn 2p spectra, one doublet peak

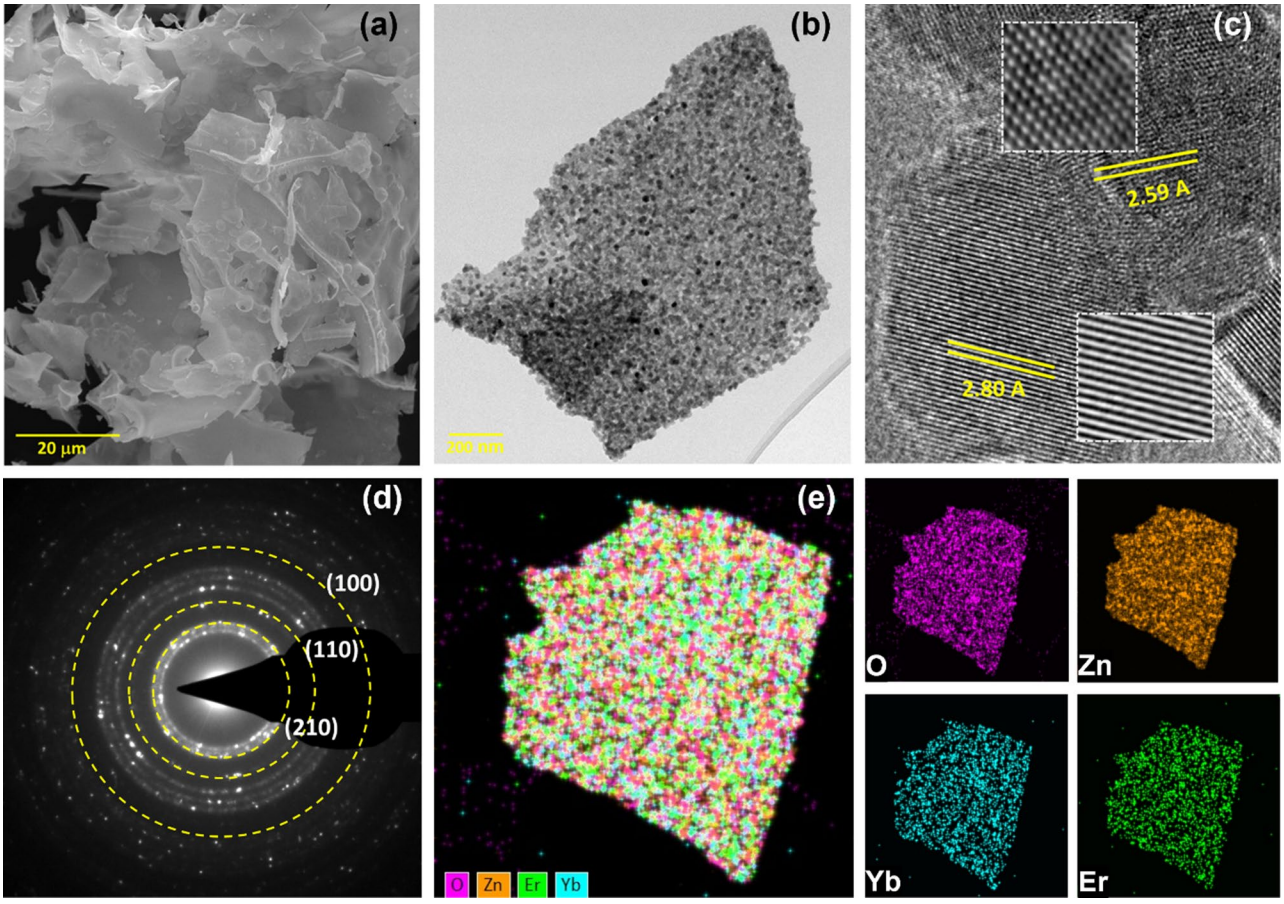

Fig. 3 (**a**) Low-magnification field-emission scanning electron microscopy (FESEM) micrograph. (**b**) Low-magnification transmission electron microscopy (TEM) micrograph. (**c**) High-resolution TEM (HRTEM) micrograph. The inset shows the inverse fast Fourier transform [IFFT] used to estimate the interplanar distance. (**d**) Selected-area electron diffraction (SAED) pattern. (**e**) Energy-dispersive X-ray spectroscopy (EDS) mapping of the ZEY NPs

(Z1) with a double Lorentzian line shape and three singlet peaks with a Gaussian line shape were used [49]. A combination of slope–SVSC backgrounds was necessary to reproduce the intensity and shape of the background. The Z1 peak located at 1021.25 eV was attributed to Zn^{2+} ions in the ZnO structure, while the singlet peaks located between 1026.50 and 1043.50 eV were ascribed to satellites (plasmon peaks) [50]. The O 1s region was fitted using two singlet peaks (Fig. 4b), associated with O^{2-} ions in ZnO and oxygen vacancies (V_O) at 530.04 (O1) and 531.62 eV (O2), respectively. Figure 4c shows the Yb 4d spectra for the ZY and ZEY powders. Notably, to adjust the Yb 4d spectrum, a wide binding energy range is necessary to correctly adjust the background and extract the chemical components associated with the spectrum. The Yb 4d spectrum generally exhibited a complex structure, with the main peak comprising multiplet-related satellites. To distinguish the oxidation states of Yb (Yb^{2+} and Yb^{3+}), it is necessary to consider that Yb^{2+} does not present multiplets, unlike Yb^{3+}, in which its partially filled 4f layer presents multiplet final-state effects [51]. The Yb 4d spectra were deconvoluted using three chemical components with a Shirley–Sherwood background. The spin–orbit separation for doublets Y1 and Y2 was 13.11 eV, while that for doublet Y3 was 11.33 eV. The three doublets, Y1 (185.52 eV), Y2 (189.69 eV), and Y3 (193.41 eV), confirmed the presence of Yb ions with an oxidation state of 3+. Meanwhile, the Er 4d spectra (Fig. 4d) were deconvoluted using a doublet with spin–orbit separation of 2.0 eV, attributed to Er^{3+} ions in ZnO. A Shirley-type background was used to reproduce the Er 4d spectra. Table 2 presents the atomic percentage (at%) of elements on the surface of the NPs. The Zn/O ratio was considerably close to unity for pure ZnO. However, the Zn/O ratio decreased upon addition of rare-earth elements (Er and Yb), indicating the formation of structural defects mainly associated with oxygen vacancies.

The oxidation states of the doping ions in the ZnO matrix are fundamental to its electronic, optical, and structural properties. The type of electronic transition that occurs in the material largely depends on these oxidation states. Doping with rare earth materials, where, normally, the oxidation state of the ions is 3+, promotes various electronic transitions that enable various

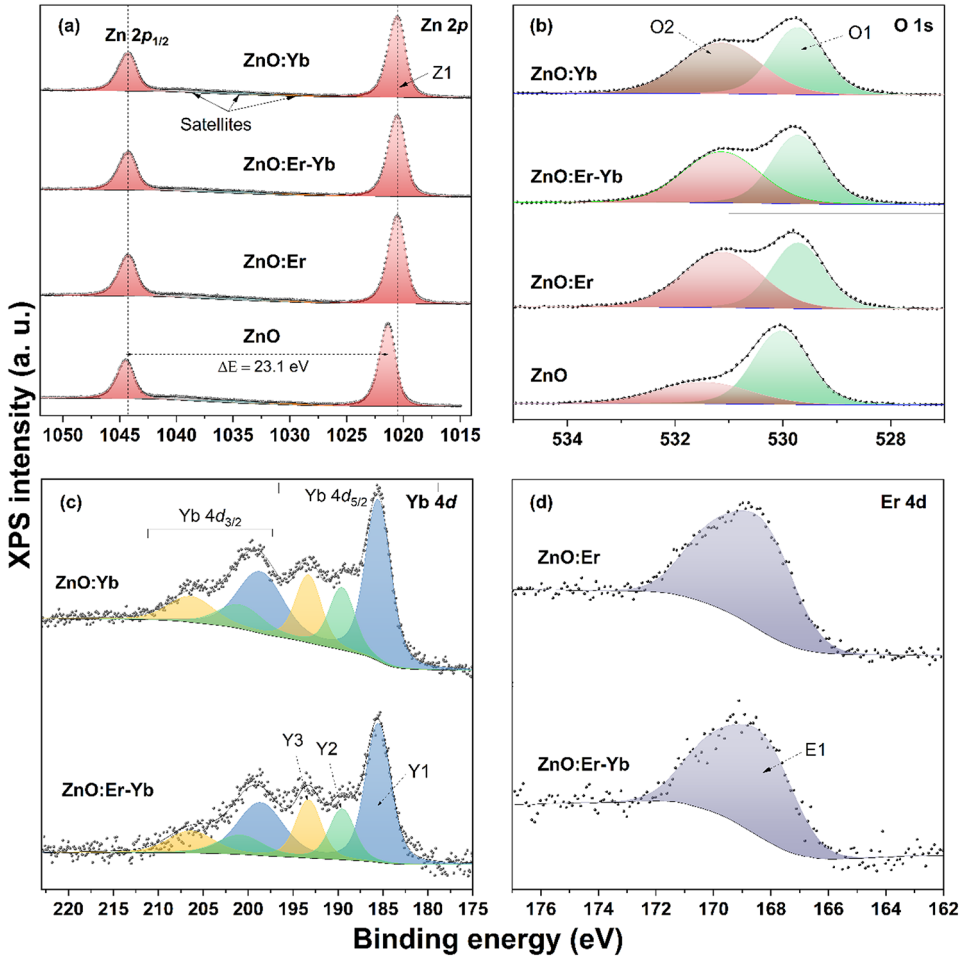

Fig. 4 High-resolution X-ray photoelectron spectroscopy (XPS) spectra of (**a**) Zn 2p, (**b**) O 1s, (**c**) Yb 4d, and (**d**) Er 4d core levels

Table 2 High-resolution X-ray photoelectron spectroscopy (XPS) spectra was used to obtain the atomic concentrations of Zn, O, Er, and Yb

Sample	Zn (at%)	O (at%)	Z1/O1	Er (at%)	Yb (at%)
ZN	25.67	25.98	0.99	-	-
ZE	18.54	19.61	0.94	1.06	-
ZEY	20.90	22.68	0.92	0.50	2.44
ZY	20.80	22.11	0.94	-	4.28

applications, such as temperature sensors, solar cells, optical storage, and green emission devices. Yb in a+2 oxidation state introduces an extra electron into the ZnO lattice, which changes its electrical properties by increasing ZnO's n-type conductivity. Yb^{3+}, the doping ion, can act as an isovalent impurity in the ZnO structure and modify the electronic band structure via interactions with other dopants or defects. Yb^{3+} ions promote the electronic transition $^2F_{5/2}$- $^2F_{7/2}$, which in coupling with Er, improves the energy transfer from Yb^{3+} to Er^{3+}. This increases the up-conversion process efficiency. Variations in the crystal structure of ZnO were observed after Er^{3+} and Yb^{3+} were incorporated (see Fig. 1b). These changes were associated with structural defects, including the formation of oxygen and zinc vacancies. Hence, the lanthanides introduced extra positive charges into the ZnO lattice. More oxygen vacancies may form to maintain charge neutrality, as each V_O can compensate for two extra positive charges (Eq. 2 and Eq. 3). Moreover, as no secondary phases were observed, and the substitution of Zn^{2+} with Er^{3+} and/or Yb^{3+} was assumed, the Zn vacancies formed as follows [52]:

$$Ln_{Zn}^{3+} + V_{Zn}^{2-} \rightarrow (Ln_{Zn} - V_{Zn})^{+} \quad (2)$$

$$(Ln - V_{zn})^{+} + V_{Zn}^{2-} \rightarrow (Ln_{Zn} - 2V_{Zn})^{-} \quad (3)$$

The defects caused by Er^{3+} and Yb^{3+} doping in ZnO play a critical role in its optoelectronic and structural properties, i.e., altering the electronic band structure by introducing localized states that promote different electronic transitions. Hence, developing metal oxide materials with defects is desirable due to their wide range of applications. For example, the antibacterial activity of ZnO in dark conditions is related to defects, not the optical band

gap [53]. Moreover, the role of Er^{3+} and/or Yb^{3+} doping in ZnO has been discussed in photovoltaic applications [54].

Cytotoxic activity

The cytotoxicity of the (Er, Yb)-doped ZnO NPs was tested using cell lines derived from major cancers including hepatocellular carcinoma, colorectal adenocarcinoma, and malignant glioma. A macrophage-derived cell line was also used to compare the cytotoxic effects of the as-prepared NMs. The cultured cell lines used were HEPG-2, RAW 264.7, CACO-2, and U87.

The HEPG-2 cell line is a widely cultured model used to investigate the potential activity of NMs against hepatocellular carcinoma. As shown in Fig. 5a, treatment with 5 µg/mL Z did not provide a cytotoxic effect against the HEPG-2 cell line. However, at 20, 50, and 100 µg/mL, Z resulted in 38.50%, 55.62%, and 72.43% cell death, respectively. The highest cytotoxicity was observed at 250 µg/mL, at which 80.77% cell death was observed. In contrast, treatment with 20 and 50 µg/mL ZE resulted in 4.03% and 4.39% cell death, respectively, whereas that with 100 and 250 µg/mL ZE caused 58.16% and 80.80% cell death, respectively. However, treatment with 5, 20, and 50 µg/mL ZEY resulted in 1.21%, 6.16%, and 30.34% cell death, respectively, and that with 100 and 250 µg/mL ZEY caused 78.82% and 78.64% cell death, respectively. Treatment with 20, 50, and 100 µg/mL ZY resulted in 4.01%, 54.71%, and 54.74% cell death, respectively, while that with 250 µg/mL ZY caused 69.13% cell death.

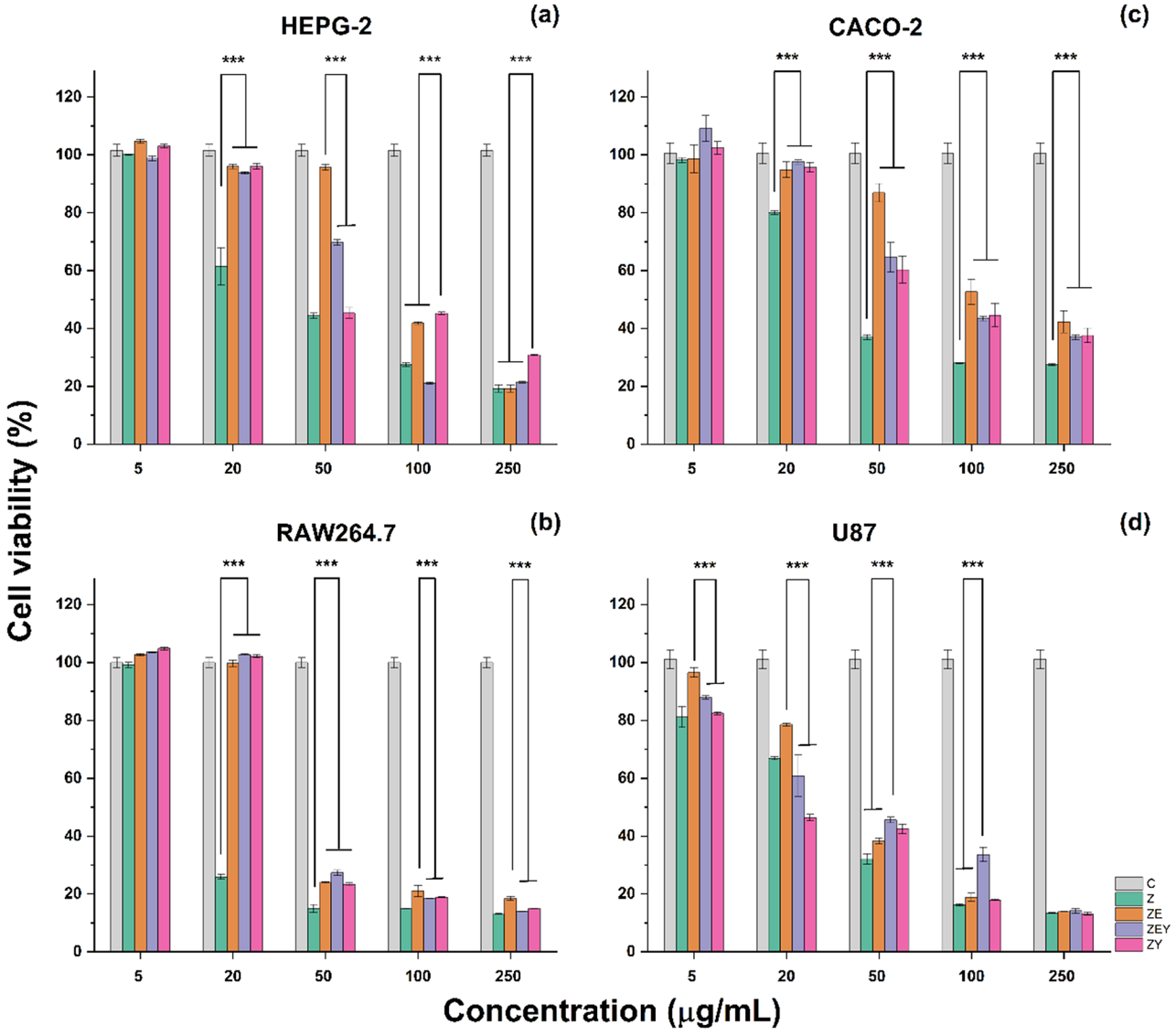

Fig. 5 Cytotoxicity of the (Er, Yb)-doped ZnO nanoparticles (NPs) against the following cell lines: (**a**) HEPG-2, (**b**) RAW264.7, (**c**) CACO-2, and (**d**) U87. The data are presented as mean ± standard deviation (SD) of three independent experiments. *$p < 0.05$, ** $p < 0.01$, and ***$p < 0.001$

In contrast with the HEPG-2 cell line, the RAW 264.7 cell line constitutes a robust model commonly employed to determine the cytotoxic effect of NMs against monocytes/macrophages. Treatment with 5, 20, and 50 µg/mL Z resulted in 0.77%, 74.09%, and 84.97% cell death, respectively (Fig. 5b). Treatment with 100 and 250 µg/mL Z caused 85.12% and 86.80% cell death, respectively. Similarly, treatment with 20, 50, and 100 µg/mL ZE resulted in 0.22%, 75.92%, and 78.93% cell death, respectively, while that with 250 µg/mL ZE caused 81.55% cell death. However, treatment with 50 µg/mL ZEY resulted in 72.60% cell death, and that with 100 and 250 µg/mL ZEY caused 81.55% and 85.93% cell death, respectively. Treatment with 50 and 100 µg/mL ZY resulted in 76.66% and 81.08% cell death, respectively, while that with 250 µg/mL ZY caused 85.10% cell death.

The CACO-2 cell line is a complex colorectal adenocarcinoma model with structural and functional features similar to those of enterocytes. Against this cell line, treatment with 5, 20, and 50 µg/mL Z resulted in 1.79%, 19.96%, and 63.03% cell death, respectively, and that with 100 and 250 µg/mL Z caused 71.97% and 72.52% cell death, respectively. Moreover, treatment with 5, 20, and 50 µg/mL ZE caused 1.37%, 5.16%, and 13.08% cell death, respectively, while that with 100 and 250 µg/mL ZE resulted in 47.32% and 57.69% cell death, respectively. Treatment with 20, 50, and 100 µg/mL ZEY caused 2.38%, 35.39%, and 56.54% cell death, respectively, and that with 250 µg/mL ZEY resulted in 62.97% cell death. Of the tested samples, ZY showed the lowest cytotoxic activity: Treatment with 5, 20, and 50 µg/mL ZY resulted in 30.18%, 39.22%, and 42.36% cell death, respectively, and that with 100 and 250 µg/mL ZY caused 47.62% and 46.52% cell death, respectively. Figure 5c shows the cytotoxicity of the (Er, Yb)-doped ZnO NPs against the CACO-2 cell line.

The cytotoxicity of the (Er, Yb)-doped ZnO NPs was also tested on the U87 cell line, which is associated with a malignant glioma cellular model. Treatment with 5, 20, and 50 µg/mL Z resulted in cell death rates of 18.76%, 33.02%, and 67.90%, respectively (Fig. 5d); higher concentrations of 100 and 250 µg/mL caused cell death rates of 83.73% and 86.59%, respectively. In contrast, treatment with 5 and 20 µg/mL ZE caused cell death rates of 3.49% and 21.46%, respectively, while that with 50, 100, and 250 µg/mL ZE induced cell death rates of 61.69%, 81.09%, and 86.14%, respectively. Treatment with 5, 20, and 50 µg/mL ZEY resulted in cell death rates of 12.13%, 39.14%, and 54.41%, respectively, while that with 100 and 250 µg/mL ZEY caused 66.33% and 85.81% cell death, respectively. Similarly, treatment with ZY showed cytotoxic effects on U87 cells: 5, 20, and 50 µg/mL ZY resulted in 17.55%, 53.58%, and 57.48% cell death, respectively, and 100 and 250 µg/mL ZY caused 82.11% and 86.83% cell death, respectively. The half-maximal inhibitory concentration (IC_{50}) values of Z, ZE, ZEY, and ZY against each cultured cell line were calculated by plotting the proportion of damaged cells against the various concentrations used (Table 3). As per the National Cancer Institute, USA, Table 3 suggests that the cytotoxicity of Z, ZE, ZEY, and ZY against the HEPG-2, CACO-2 and U87 cell lines can be considered moderate. Similarly, the cytotoxicity of ZE, ZEY, and ZY against RAW 264.7 cells can be regarded as moderate, except for Z, which exhibited a high cytotoxicity activity. Figure 6 depicts the possible mechanisms by which the (Er, Yb)-doped ZnO NPs decreased the viability of the cultured cancer cell lines.

Table 3 Half-maximal inhibitory concentration (IC_{50}) values (in µg/mL) of Z, ZE, ZEY, and ZY against the HEPG-2, RAW 264.7, CACO-2, and U87 cell lines

Sample	HEPG-2	RAW 264.7	CACO-2	U87
Z	87.15	2.05	102.30	51.95
ZE	114.57	95.40	190.64	82.43
ZEY	119.17	94.55	160.68	78.66
ZY	138.75	92.87	263.05	41.76

The recent studies have shown that ZnO NPs can induce cell death in cancer cell lines via various mechanisms. For instance, ZnO NPs synthesized with *Boerhaavia diffusa* extract have been observed to decrease the viability of HEPG-2 cells in a dose-dependent manner (25–100 µg/mL) by increasing the production of ROS and reactive nitrogen species, disrupting the mitochondrial membrane potential (ΔΨm 1359) and upregulating the caspase 3/7 activity [55]. Similarly, ZnO NPs prepared via a solution combustion method have been reported to decrease the viability of a human malignant glioma cell line (LN-18) within the concentration range of 3.12–200 µg/mL, partially associated with the determined small size and spherical of the synthesized ZnO NPs.

Conversely, Er_2O_3 NPs have been observed to reduce the viability of HEPG-2 cells by arresting their cell cycle at the G0/G1 phase, upregulating apoptotic genes (p53 and Bax), inducing DNA damage, and facilitating the generation of intracellular ROS [56]. Similarly, ZnO NPs doped with Yb^{3+} and Ce have been reported to induce cell death in HCT-116 colon cancer cells by inducing chromatin condensation and fragmentation [21]. In contrast, Er_2O_3 NPs have not been observed to induce considerable morphological changes, genetic material damage, or apoptosis gene expression changes in human skin fibroblasts (HSFs), although they did reduce the viability of HSF cells post 72 h of exposure [19]. The variabilities between these findings and this study's results can be attributed to difference in synthesis route, morphological features, size, lattice structure, and concentrations of the respective (Er, Yb)-doped ZnO NPs used.

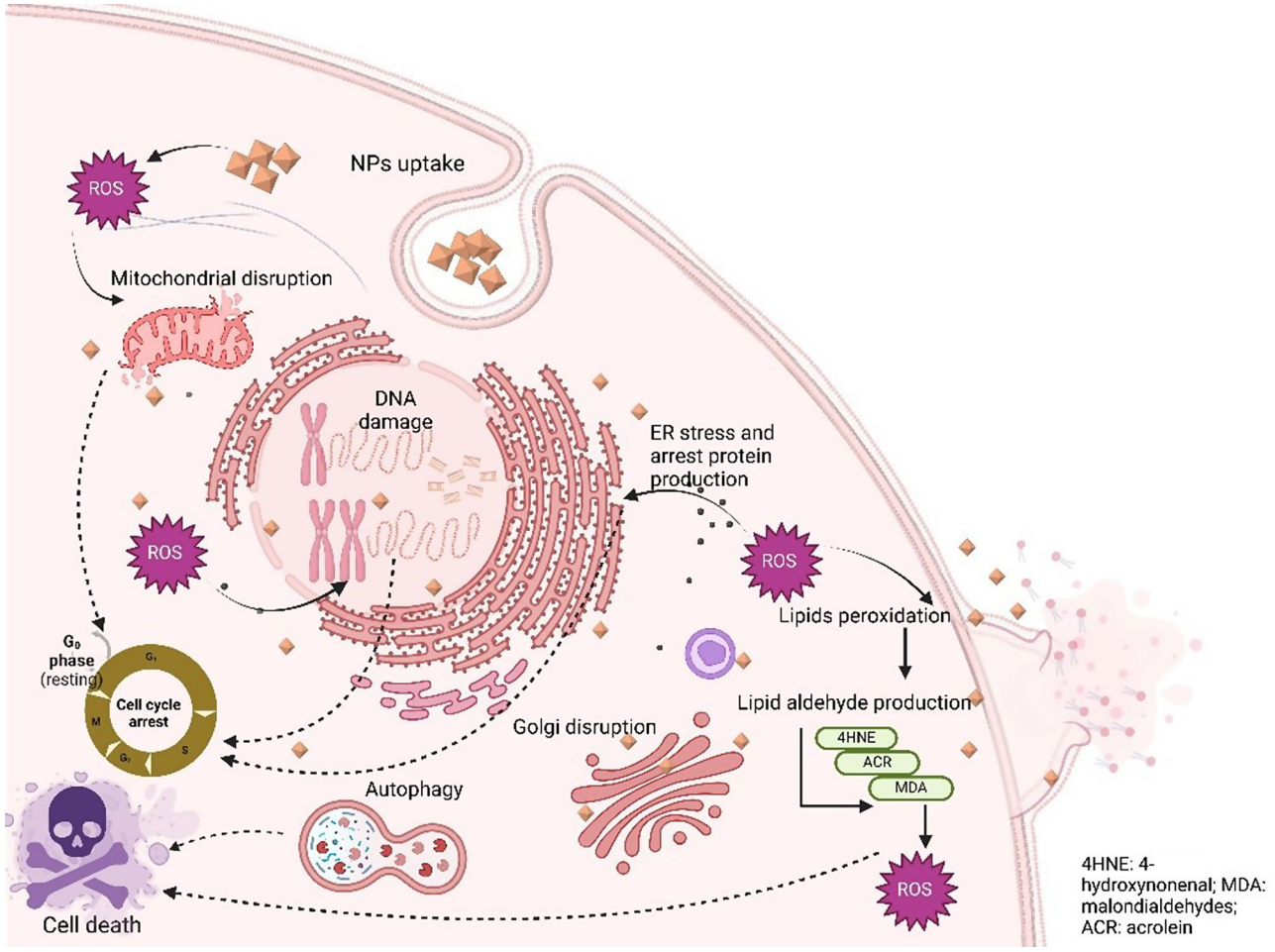

Fig. 6 Possible anticancer mechanisms of the (Er, Yb)-doped ZnO nanoparticles (NPs)

Antioxidant activity

The antioxidant activity of synthetic materials can be measured using various techniques involving chemical reactions measured spectrophotometrically, interpreted quantitatively, and monitored qualitatively. Accordingly, we employed the DPPH, ABTS, and H_2O_2 assays to evaluate the free radical inhibition ability of the (Er, Yb)-doped ZnO NPs, which were further compared with the of ascorbic acid (AC) activity. Among natural antioxidants, AC is a water-soluble vitamin that regulates collagen synthesis [57], immune system response [58], cell proliferation and differentiation [59], and cytokine production [60]. AC is a valuable therapeutic source against oxidative stress-related disorders since it can effectively neutralize the generation of free radicals (e.g., OH, $^1O_2$, and H_2O_2) involved in disease progression, such as Alzheimer's disease [61], hepatocellular carcinoma [62], and neuroinflammation [63].

DPPH assay

The DPPH radical is a stable molecule that is violet in color and possesses hydrogen acceptor capability. It is widely used to investigate the antioxidant activity of natural and synthetic antioxidants because of its high sensitivity and minimal sample preparation requirements [32]. As shown in Fig. 7a, treatment with 5, 20, and 50 µg/mL Z scavenged 51.66%, 52.24%, and 55.52% of DPPH radicals, respectively, while 100 µg/mL Z inhibited 64.62% of free radicals. Similarly, 5 and 20 µg/mL ZE scavenged 45.25% and 51.62% of radicals, respectively, whereas 50 and 100 µg/mL ZE inhibited 51.77% and 52.48% of radicals, respectively. However, treatment with 5, 20, and 50 µg/mL ZEY scavenged 53.92%, 56.01%, and 59.84% of DPPH radicals, respectively, while 100 µg/mL ZEY inhibited 59.84% of free radicals. Similarly, ZY at 5 and 20 µg/mL scavenged 55.07% and 55.73% of radicals, respectively, whereas 50 and 100 µg/mL ZY inhibited 55.52% and 64.62% of DPPH radicals, respectively.

We demonstrated that ZnO-based NPs at various concentrations can successfully scavenge DPPH radicals under various conditions. For instance, Er_2O_3 NPs synthesized from *Hyphaene thebaica* extracts disrupted 28.31–66.25% of DPPH radicals when used at 62.5–1000 µg/mL [17]. Similarly, Yb_2O_3 NPs synthesized from

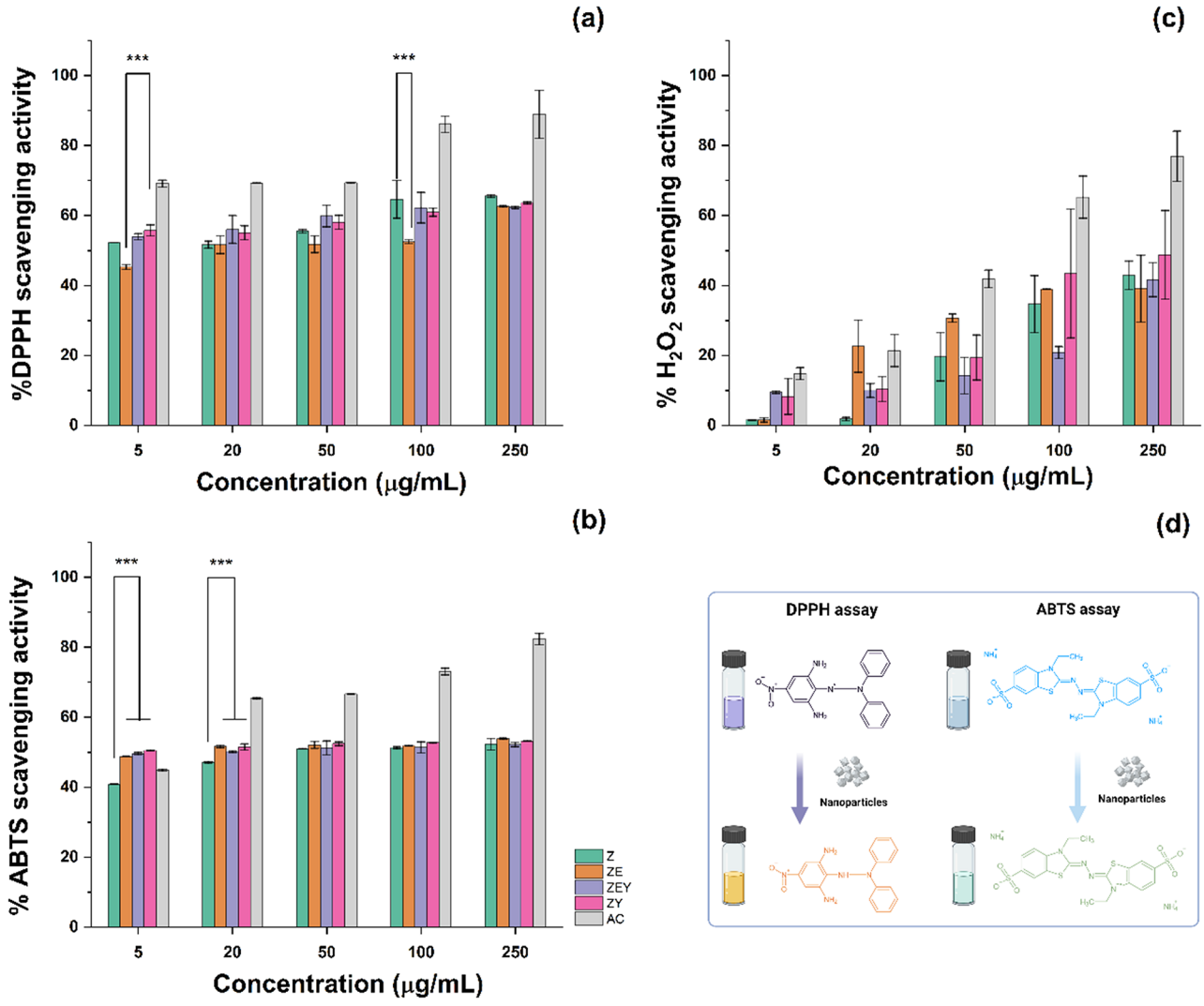

Fig. 7 Antioxidant activity of (Er, Yb)-doped ZnO NPs against (**a**) 2,2-diphenyl-1-picrylhydrazyl (DPPH), (**b**) 2,2′-azino-bis(3-ethylbenzothiazoline-6-sulfonic acid (ABTS), (**c**) H2O2 radicals, and (**d**) their possible mechanisms. The terms Z, ZE, ZEY, and ZY are associated with the developed materials in this study. AC represents ascorbic acid, the positive control for these assays. The data are presented as the means ± standard deviation (SD) of three independent experiments. * $p < 0.05$, ** $p < 0.01$, and *** $p < 0.001$

Andrographis paniculata leaf extract inhibited 16.33–56.13% of DPPH radicals when used at 50–500 µg/mL. Despite differences in physicochemical and optical properties, the antioxidant activity of ZnO NPs doped with Er^{3+} or Yb^{3+} is attributed to electron transfer from the oxygen atom of ZnO to the unpaired electron localized on the nitrogen atom of DPPH free radicals (Fig. 7d).

ABTS assay

The ABTS assay is a colorimetric technique in which the ABTS radical cation is decolorized from deep to pale blue green in the presence of antioxidants. This assay provides valuable information about the antioxidant activity of synthetic materials because of its high sensitivity, versatility, and complementarity with other antioxidant assays. Treatment with 5, 20, and 50 µg/mL Z scavenged 40.80%, 47.09%, and 50.87% of ABTS radicals, respectively (Fig. 7b). Z at 100 and 250 µg/mL inhibited 51.23% and 52.22% of free radicals, respectively. In contrast, ZE at 5 and 20 µg/mL inhibited 48.68% and 51.56% of ABTS radicals, respectively, while ZE at 50, 100, and 250 µg/mL scavenged 51.78%, 52.01%, and 53.82% of radicals, respectively. However, treatment with 5, 20, and 50 µg/mL ZEY scavenged 49.51%, 50.13%, and 51.14% of ABTS radicals, respectively, and treatment with 100 and 250 µg/mL ZEY inhibited 51.31% and 52.16% of free radicals, respectively. However, ZY at 5 and 20 µg/ mL inhibited 50.41% and 51.41% of radicals, respectively, whereas ZY at 50, 100, and 250 µg/mL scavenged 52.38%, 52.71%, and 53.11% of free radicals, respectively.

There have been limited reports on the antioxidant activity of (Er, Yb)-doped ZnO NPs against ABTS

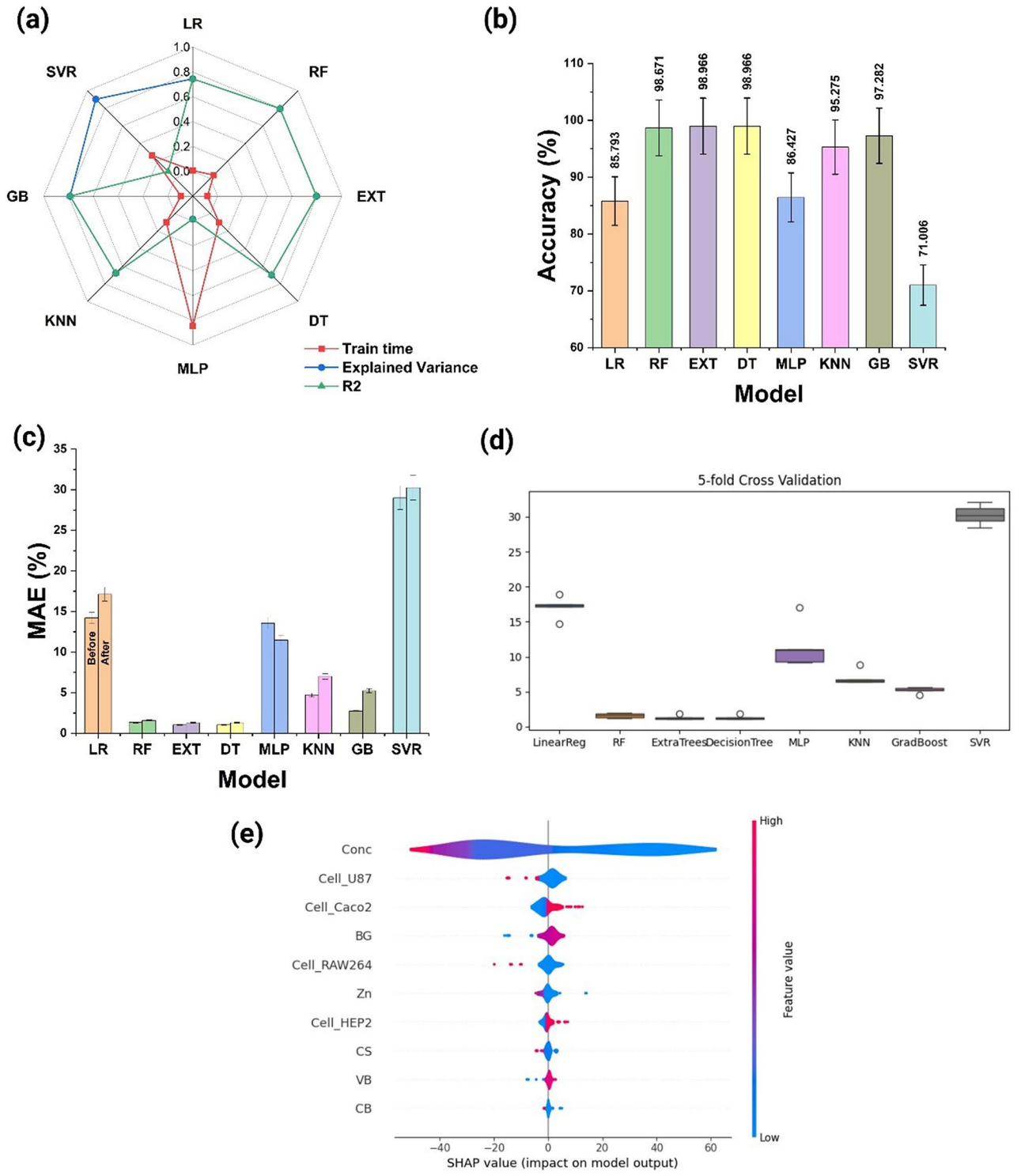

Fig. 8 Overview of the machine learning (ML) experiment findings. **a**–**c**): Various metrics for model quality assessment. **d**) Outcomes of performing five repeated procedures. **e**) Feature importance assessment for the best performing model

radicals. Although this study is the first to evaluate (Er, Yb)-doped ZnO NPs using the ABTS assay, it is already known that lanthanide-based NMs can scavenge free radicals because of their 4f shielded electrons, doping content, and structural arrangement [31]. The ability of ZnO NPs to neutralize ABTS radicals may be associated with their capacity to donate hydrogen atoms [64].

H2O2 assay

Unlike DPPH and ABTS radicals, H_2O_2 radicals are strong oxidants that can be detected spectrophotometrically [65], fluorometrically [66], or electrochemically [67] in various samples. H_2O_2 naturally occurs in human cells and is involved in both healthy cellular processes and pathological oxidative stress. As shown in Fig. 7c, treatment with 5 and 20 µg/mL Z scavenged 1.45% and 1.82% of H_2O_2 radicals, respectively, whereas treatment with 50, 100, and 250 µg/mL Z inhibited 19.6%, 34.67%, and 42.90% of radicals, respectively. Similarly, ZE at 5, 20, and 50 µg/mL inhibited 1.49%, 22.57%, and 30.67% of free radicals, respectively, and ZE at 100 and 250 µg/mL scavenged 38.94% and 39.07% of H_2O_2 radicals, respectively. Treatment with 5, 20, and 50 µg/mL ZEY inhibited 9.46%, 9.94%, and 14.23% of free radicals, respectively, while 100 and 250 µg/mL ZEY scavenged 30.83% and 41.65% of H_2O_2 radicals, respectively. Finally, ZY exhibited the highest antioxidant activity against H_2O_2 radicals, scavenging 8.24%, 10.33%, and 19.38% of radicals at 5, 20, and 50 µg/mL, respectively, and inhibiting 43.47% and 48.72% at 100 and 250 µg/mL, respectively. Unfortunately, limited evidence exists on the capacity of ZnO-based NMs to scavenge H_2O_2 despite its role in disease progression. The antioxidant activity observed in this study can be correlated to the high surface area and reactive surface sites of NMs that interact with and neutralize H_2O_2 radical formation [68]. Although the specific mechanisms for Er_2O_3 or Yb_2O_3 NMs against H_2O_2 radicals are not well documented, lanthanide-based NPs can stimulate endogenous antioxidant enzymes such as superoxide dismutase and catalase to facilitate the decomposition of H_2O_2 into water and oxygen, thereby reducing oxidative stress [69].

ML modeling

Figure 8a shows the results of the ML model training time, explained variance, and correlation coefficient or determination coefficient with default parameters. The EXT and DT models performed best, each with a 1% prediction error (Fig. 8b). In contrast, SVR had the highest error rate (29%).

Figure 8c shows the mean absolute error (MAE) of each model, exhibiting a pattern similar to that of the accuracy measure. After five-fold cross-validation, as illustrated in Fig. 8d, DT and EXT continued leading with an error rate of 1.3% error, whereas the SVR lagging at 30% error. The minimal standard deviation in errors across the models indicates stable and consistent predictive performance. Figure 8e shows the SHAP values for the top 10 contributing features. The concentration was the most crucial variable, followed by cell line CACO-2, cell line U87, BG (optical bandgap), and cell line RAW264.7. Each point on the graph indicates a dataset observation, with the horizontal axis representing SHAP values and color indicating higher or lower values. High concentrations negatively affected the model's predictions, whereas low concentrations had a positive influence. The CACO-2 and U87 cell lines exhibited contrasting influences: high CACO-2 values positively influenced the model, low values were detrimental, and the opposite was true for the U87 cell line. These differences are attributed to the molecular and cellular complexity of the CACO-2 and U87 cell lines, which considerably influences the cytotoxicity of the developed NMs.

Conclusions

(Er, Yb)-doped ZnO NPs were successfully synthesized and characterized using spectroscopy (UV–Vis, FTIR, XRD, EDS, and HR-XPS) and microscopy (TEM/HRTEM/STEM) techniques. The NPs were evaluated for their anticancer and antioxidant properties and used for ML model training. The characterization revealed that doping with Er^{3+} and Yb^{3+} decreased crystallinity, modified TC, and altered absorbance capacity in laminar-type structures. The optical bandgaps of Z, ZE, ZEY, and ZY were 3.20, 3.22, 3.24, and 3.23 eV, respectively, which influenced their anticancer and antioxidant activities. Z exhibited the highest anticancer activity against the HEPG-2, CACO-2, and U87 cell lines with an IC_{50} of <102.30 µg/mL, whereas ZY exhibited the lowest activity, with an IC_{50} of <263.05 µg/mL. Despite this event, it was noted that the cytotoxicity of the obtained materials was also higher or moderate towards RAW 264.7 cells (IC_{50} 2.05–95.40 µg/mL), a macrophage-derived cell line frequently involved in immunological responses. Therefore, further approaches are required to develop alternatives that aid the preservation of the capacity of (Er, Yb)-doped ZnO NPs to be implemented in cancer therapy while reducing their toxicity. Even though no statistical differences were observed when compared to treatment with AC, lanthanide doping increased the ZnO NPs' capacity to scavenge DPPH, ABTS, and H_2O_2 radicals at concentrations of 5–250 µg/mL, which is of significant importance since it demonstrates the potential of Z, ZE, ZEY, and ZY to act as efficient antioxidant systems with the capacity to be implemented in the treatment of oxidative-stress related disorders such as neurodegeneration, cancer, and metabolic diseases. Among the ML models trained, EXT and DT models achieved accuracies of 98.96% and MAEs of 1.30%, effectively illustrating the effect of concentration and cell line type on the performance of (Er, Yb)-doped ZnO NPs. This study provides new insights into the nanobiotechnological applications of these NPs for the first time, advancing our knowledge of UPNPs and ML modeling, and highlighting the importance of optical bandgaps in the cytotoxicity and antioxidant properties of NMs.

Acknowledgements
This research was partially funded by the Challenge-Based Research Funding Program 2022 and the Nanodevices Research Group at Tecnologico de Monterrey. The authors acknowledge COECYTJAL for partial funding through the FODECIJAL 2023 Program.

Author contributions
Jorge L. Mejía-Méndez: Conceptualization, Methodology, Formal Analysis, Investigation, Writing–Original Draft, Writing–Review & Editing.Edwin E. Reza-Zaldívar: Conceptualization, Methodology, Formal Analysis, Investigation, Writing–Original Draft, Writing–Review & Editing. A. Sanchez-Martinez: Writing–Review & Editing.O. Ceballos-Sanchez: Writing–Review & Editing. Diego E. Navarro-López: Writing–Review & Editing.L. Marcelo Lozano: Writing–Review & Editing.Juan Armendariz-Borunda: Writing–Review & Editing. Naveen Tiwari: Conceptualization: Formal Analysis, Writing–Review & Editing. Daniel A. Jacobo-Velázquez: Conceptualization, Software, Investigation, Writing–Original Draft, Writing–Review & Editing, Resources, Supervision, and Project Administration.Gildardo Sanchez-Ante: Conceptualization, Software, Investigation, Writing–Original Draft, Writing–Review & Editing, Resources, Supervision, and Project Administration.Edgar R. López-Mena: Conceptualization, Software, Investigation, Writing–Original Draft, Writing–Review & Editing, Resources, Supervision, and Project Administration.

Funding
Not applicable.

Data availability
No datasets were generated or analysed during the current study.

Declarations

Ethics approval and consent to participate
Not applicable.

Consent for publication
Not applicable.

Competing interests
The authors declare no competing interests.

Author details
[1]Departamento de Ciencias Químico-Biológicas, Universidad de las Américas Puebla, Santa Catarina Mártir s/n, Cholula, Puebla 72810, Mexico
[2]Tecnologico de Monterrey, Institute for Obesity Research, Ave. General Ramon Corona 2514, Zapopan, Jalisco 45201, Mexico
[3]Departamento de Ingeniería de Proyectos, CUCEI, Universidad de Guadalajara, Av. José Guadalupe Zuno # 48, Industrial los Belenes, Zapopan, Jalisco 45157, México
[4]Tecnologico de Monterrey, Escuela de Ingenieria y Ciencias, Ave. General Ramon Corona 2514, Zapopan, Jalisco 45138, Mexico
[5]Tecnologico de Monterrey, School of Medicine and Health Sciences, Ave. General Ramon Corona 2514, Zapopan, Jalisco 45138, Mexico
[6]Institute for Molecular Biology in Medicine and Gene Therapy, Department of Molecular Biology and Genomics, Health Sciences University Center, University of Guadalajara, Guadalajara 44340, Mexico
[7]Center for Research in Biological Chemistry and Molecular Materials (CiQUS), , University of Santiago de Compostela, Rúa Jenaro de La Fuente S/N, 15782, Santiago de Compostela, A Coruna 15782, Mexico

Received: 19 August 2024 / Accepted: 27 October 2024
Published online: 10 November 2024

References

1. Salari N, Ghasemi H, Fatahian R, Mansouri K, Dokaneheifard S, Shiri MH, Hemmati M, Mohammadi M. The global prevalence of primary central nervous system tumors: a systematic review and meta-analysis. Eur J Med Res. 2023;28:39.
2. Sung H, Ferlay J, Siegel RL, Laversanne M, Soerjomataram I, Jemal A, Bray F. Global Cancer Statistics 2020: GLOBOCAN Estimates of Incidence and Mortality Worldwide for 36 Cancers in 185 Countries. CA Cancer J Clin. 2021;71:209–49.
3. Chen B, Chen C, Zhang Y, Xu J. Recent incidence trend of elderly patients with glioblastoma in the United States, 2000–2017. BMC Cancer. 2021;21:54.
4. Al Bitar M, Hassanieh B, Awad R, Khalil M. Characterization and evaluation of the therapeutic benefits of pure and lanthanides mono- and co-doped zinc oxide nanoparticles. Saudi J Biol Sci. 2023;30:103608.
5. Liu C, Pang M, Wang Q, Yan M, Zhou Y, Yao H, Du B. Intestinal Absorption of Nanoparticles to Reduce Oxidative Stress and Vasoconstriction for Treating Diabetic Nephropathy. ACS Biomater Sci Eng. 2024;10:1517–29.
6. Jia W, Guo A, Zhang R, Shi L. Mechanism of natural antioxidants regulating advanced glycosylation end products of Maillard reaction. Food Chem. 2023;404:134541.
7. Singh TA, Sharma A, Tejwan N, Ghosh N, Das J, Sil PC. A state of the art review on the synthesis, antibacterial, antioxidant, antidiabetic and tissue regeneration activities of zinc oxide nanoparticles. Adv Colloid Interface Sci. 2021;295:102495.
8. Zhao T, Wu W, Sui L, Huang Q, Nan Y, Liu J, Ai K. Reactive oxygen species-based nanomaterials for the treatment of myocardial ischemia reperfusion injuries. Bioact Mater. 2022;7:47–72.
9. Wei HL, Zheng W, Zhang X, Suo H, Chen B, Wang Y, Wang F. Tuning Near-Infrared-to-Ultraviolet Upconversion in Lanthanide-Doped Nanoparticles for Biomedical Applications. Adv Opt Mater 2022, 11, 2201716.
10. Wu F, Chen H, Li Q, Liu R, Suo Y, Li B, Kong X, Cheng Z, Liu H, Chang Y. Amplifying oxidative stress utilizing multiband luminescence of lanthanide nanoparticles for eliciting systemic antitumor immunity. Chem Eng J 2023, 468, 143827.
11. Cressoni C, Vurro F, Milan E, Muccilli M, Mazzer F, Gerosa M, Boschi F, Spinelli AE, Badocco D, Pastore P, et al. From Nanothermometry to Bioimaging: Lanthanide-Activated KY(3)F(10) Nanostructures as Biocompatible Multifunctional Tools for Nanomedicine. ACS Appl Mater Interfaces. 2023;15:12171–88.
12. Liu L, Shi J, Peng S, Zhong H, Lin P, Wang J, Sun X, Song L, Yuan Q, Zhang Y. Biodegradable near-infrared-IIb lanthanide-doped inorganic nanoparticles with red up-conversion luminescence for bioimaging and photodynamic therapy. Sci China Mater. 2023;66:2893–901.
13. Navarro-Lopez DE, Garcia-Varela R, Ceballos-Sanchez O, Sanchez-Martinez A, Sanchez-Ante G, Corona-Romero K, Buentello-Montoya DA, Elias-Zuniga A, Lopez-Mena ER. Effective antimicrobial activity of ZnO and Yb-doped ZnO nanoparticles against Staphylococcus aureus and Escherichia coli. Mater Sci Eng C Mater Biol Appl. 2021;123:112004.
14. Alenazi DAK. Development of color-tunable photoluminescent polycarbonate smart window immobilized with silica-coated lanthanide-activated strontium aluminum oxide nanoparticles. Inorg Chem Commun 2023, 150, 110473.
15. Alotaibi MO, Alotaibi NM, Ghoneim AM, Ain NU, Irshad MA, Nawaz R, Abbas T, Abbas A, Rizwan M, Ali S. Effect of green synthesized cerium oxide nanoparticles on fungal disease of wheat plants: A field study. Chemosphere. 2023;339:139731.
16. Zuo J, Tu L, Li Q, Feng Y, Que I, Zhang Y, Liu X, Xue B, Cruz LJ, Chang Y, et al. Near Infrared Light Sensitive Ultraviolet-Blue Nanophotoswitch for Imaging-Guided Off-On Therapy. ACS Nano. 2018;12:3217–25.
17. Mohamed HEA, Khalil AT, Hkiri K, Ayaz M, Abbasi JA, Sadiq A, Ullah F, Nawaz A, Ullah I, Maaza M. Physicochemical and nanomedicine applications of phyto-reduced erbium oxide (Er(2)O(3)) nanoparticles. AMB Express. 2023;13:24.
18. Jamil M, Mustafa IS, Sahul Hamid SB, Ahmed NM, Khazaalah TH, Godwin E, Ezra NS, Salah HN. Parameterisation and cellular evaluation of poly(ethylene) oxide-coated erbium oxide in MCF-7 cells as MRI diagnostic nanofibres. Colloids Surf B Biointerfaces. 2023;228:113423.
19. Mohamed HRH, Ibrahim MMH, Soliman ESM, Safwat G, Diab A. Estimation of Calcium Titanate or Erbium Oxide Nanoparticles Induced Cytotoxicity and Genotoxicity in Normal HSF Cells. Biol Trace Elem Res. 2023;201:2311–8.
20. Muthulakshmi V, Sundrarajan M. Green synthesis of ionic liquid assisted ytterbium oxide nanoparticles by Couroupita guianensis abul leaves extract for biological applications. J Environ Chem Eng 2020, 8, 103992.
21. Hannachi E, Khan FA, Slimani Y, Rehman S, Trabelsi Z, Akhtar S, Al-Suhaimi EA. In Vitro Antimicrobial and Anticancer Peculiarities of Ytterbium and Cerium Co-Doped Zinc Oxide Nanoparticles. Biology (Basel) 2022, 11 (12), 1836.
22. Albalwi HA, El-Naggar ME, Taleb MA, Kalam A, Alghamdi NA, Mostafa MS, Salem S, Afifi M. Medical applications of ternary nanocomposites based on hydroxyapatite/ytterbium oxide/graphene oxide: potential bone tissue engineering and antibacterial properties. J Mater Res Technol. 2022;18:4834–45.

23. Kumar P, Inwati GK, Mathpal MC, Ghosh S, Roos WD, Swart HC. Defects induced enhancement of antifungal activities of Zn doped CuO nanostructures. Appl Surf Sci 2021, 560, 150026.
24. Krishna MS, Singh S, Batool M, Fahmy HM, Seku K, Shalan AE, Lanceros-Mendez S, Zafar MN. A review on 2D-ZnO nanostructure based biosensors: from materials to devices. Mater Adv. 2023;4:320–54.
25. Kumar P, Kumar A, Rizvi MA, Moosvi SK, Krishnan V, Duvenhage MM, Roos WD, Swart HC. Surface, optical and photocatalytic properties of Rb doped ZnO nanoparticles. Appl Surf Sci 2020, 514, 145930.
26. Pathak TK, Kroon RE, Craciun V, Popa M, Chifiriuc MC, Swart HC. Influence of Ag, Au and Pd noble metals doping on structural, optical and antimicrobial properties of zinc oxide and titanium dioxide nanomaterials. Heliyon. 2019;5:e01333.
27. Indumathi T, Theivarasu C, Pradeep I, Rani MT, Magesh G, Rahale CS, Kumar ER. Effects of Nd doping on structural, optical, morphological and surface-chemical state analysis of ZnO nanoparticles for antimicrobial and anticancer activities. Surf Interfaces 2021, 23, 101000.
28. Du K, Feng J, Gao X, Zhang H. Nanocomposites based on lanthanide-doped upconversion nanoparticles: diverse designs and applications. Light Sci Appl. 2022;11:222.
29. Krenn M, Pollice R, Guo SY, Aldeghi M, Cervera-Lierta A, Friederich P, Dos Passos Gomes G, Hase F, Jinich A, Nigam A, et al. On scientific understanding with artificial intelligence. Nat Rev Phys. 2022;4:761–9.
30. Perfecto-Avalos Y, Navarro-López DE, Martínez-Beltrán S, Rojas-Torres DE, Suárez Ávila KD, Robles I, Zavala T, de Luna A, Sanchez-Martinez MA, Ceballos-Sanchez A. Data-Driven Machine Learning to Predict Antibacterial Activity of Cerium-Doped Nanoparticles. ACS Appl Nano Mater. 2023;6:20719–30.
31. Ceballos-Sanchez O, Navarro-Lopez DE, Mejia-Mendez JL, Sanchez-Ante G, Rodriguez-Gonzalez V, Sanchez-Lopez AL, Sanchez-Martinez A, Duron-Torres SM, Juarez-Moreno K, Tiwari N, Lopez-Mena ER. Enhancing antioxidant properties of CeO(2) nanoparticles with Nd(3+) doping: structural, biological, and machine learning insights. Biomater Sci. 2024;12:2108–20.
32. Mejia-Mendez JL, Navarro-Lopez DE, Sanchez-Martinez A, Ceballos-Sanchez O, Garcia-Amezquita LE, Tiwari N, Juarez-Moreno K, Sanchez-Ante G, Lopez-Mena ER. Lanthanide-Doped ZnO Nanoparticles: Unraveling Their Role in Cytotoxicity, Antioxidant Capacity, and Nanotoxicology. Antioxid (Basel) 2024, 13 (2), 213.
33. Sarker IH. Deep Learning: A Comprehensive Overview on Techniques, Taxonomy, Applications and Research Directions. SN Comput Sci. 2021;2:420.
34. Choudhary K, DeCost B, Chen C, Jain A, Tavazza F, Cohn R, Park CW, Choudhary A, Agrawal A, Billinge SJL et al. Recent advances and applications of deep learning methods in materials science. npj Comput Mater 2022, 8, 59.
35. Herrera-Gomez A, Bravo-Sanchez M, Ceballos-Sanchez O, Vazquez-Lepe MO. Practical methods for background subtraction in photoemission spectra. Surf Interface Anal. 2014;46:897–905.
36. Lundberg SM, Lee S-I. A unified approach to interpreting model predictions. In *Proceedings of the 31st International Conference on Neural Information Processing Systems*. pp. 4768–4777. Long Beach, California, USA: Curran Associates Inc.; 2017:4768–4777.
37. Peters JA, Djanashvili K, Geraldes CFGC, Platas-Iglesias C. The chemical consequences of the gradual decrease of the ionic radius along the Ln-series. Coord Chem Rev 2020, 406, 213146.
38. Ayu DG, Gea S, Andriayani, Telaumbanua DJ, Piliang AFR, Harahap M, Yen Z, Goei R, Tok AIY. Photocatalytic Degradation of Methylene Blue Using N-Doped ZnO/Carbon Dot (N-ZnO/CD) Nanocomposites Derived from Organic Soybean. ACS Omega. 2023;8:14965–84.
39. Mi C, Wu J, Yang Y, Han B, Wei J. Efficient upconversion luminescence from Ba5Gd8Zn4O21:Yb(3+), Er(3+) based on a demonstrated cross-relaxation process. Sci Rep. 2016;6:22545.
40. Dubey N, Chandra S. Upconversion nanoparticles: Recent strategies and mechanism based applications. J Rare Earths. 2022;40:1343–59.
41. Krajewski M, Tokarczyk M, Swietochowski P, Wrobel P, Kaminska M, Drabinska A. Structural, Optical, and Electrical Properties of Hafnium-Aluminum-Zinc-Oxide Films Grown by Atomic Layer Deposition for TCO Applications. ACS Omega. 2023;8:30621–9.
42. Jiménez JA. Physical and spectroscopic properties of variable Yb2O3 doped phosphate glasses containing SnO as UV sensitizer for Yb3 + NIR emission. Opt Mater 2023, 141, 113984.
43. Landi S, Segundo IR, Freitas E, Vasilevskiy M, Carneiro J, Tavares CJ. Use and misuse of the Kubelka-Munk function to obtain the band gap energy from diffuse reflectance measurements. Solid State Commun 2022, 341, 114573.
44. Sánchez-López AL, Perfecto-Avalos Y, Sanchez-Martinez A, Ceballos-Sanchez O, Sepulveda-Villegas M, Rincón-Enríquez G, Rodríguez-González V, Garcia-Varela R, Lozano LM, Eloyr Navarro-López D et al. Influence of erbium doping on zinc oxide nanoparticles: Structural, optical and antimicrobial activity. Appl Surf Sci 2022, 575, 151764.
45. Baldovino-Medrano VG, Niño-Celis V, Isaacs Giraldo R. Systematic Analysis of the Nitrogen Adsorption–Desorption Isotherms Recorded for a Series of Materials Based on Microporous–Mesoporous Amorphous Aluminosilicates Using Classical Methods. J Chem Eng Data. 2023;68:2512–28.
46. Hannachi E, Slimani Y, Nawaz M, Sivakumar R, Trabelsi Z, Vignesh R, Akhtar S, Almessiere MA, Baykal A, Yasin G. Preparation of cerium and yttrium doped ZnO nanoparticles and tracking their structural, optical, and photocatalytic performances. J Rare Earths. 2023;41:682–8.
47. Weiss M, Fan J, Claudel M, Sonntag T, Didier P, Ronzani C, Lebeau L, Pons F. Density of surface charge is a more predictive factor of the toxicity of cationic carbon nanoparticles than zeta potential. J Nanobiotechnol. 2021;19:5.
48. Ruhle B, Krumrey JF, Hodoroaba VD. Workflow towards automated segmentation of agglomerated, non-spherical particles from electron microscopy images using artificial neural networks. Sci Rep. 2021;11:4942.
49. Herrera-Gomez A, Guzman-Bucio DM, Carmona-Carmona AJ, Cortazar-Martinez O, Mayorga-Garay M, Cabrera-German D, Ospina-Ocampo CA, Crist BV, Raboño-Borbolla J. Double Lorentzian lineshape for asymmetric peaks in photoelectron spectroscopy. J Vacuum Sci Technol A 2023, 41, 043208.
50. Frankcombe TJ, Liu Y. Interpretation of Oxygen 1s X-ray Photoelectron Spectroscopy of ZnO. Chem Mater. 2023;35:5468–74.
51. Engel S, Gießelmann ECJ, Reimann MK, Pöttgen R, Janka O. On the Ytterbium Valence and the Physical Properties in Selected Intermetallic Phases. ACS Organic & Inorganic Au; 2024.
52. Li WL, Hou QY, Jia XF, Xu ZC. Effects of La Doping and Zn or O Vacancy on the Magnetic Property of ZnO. J Supercond Novel Magn. 2018;31:3297–305.
53. Johnson D, Reeks JM, Caron A, Tzoka I, Ali I, McGillivray SM, Strzhemechny YM. Influence of Surface Properties and Microbial Growth Media on Antibacterial Action of ZnO. Coatings 2022, 12 (11), 1648.
54. Derouiche M, Salhi R, Baklouti S. Efficient Up-Conversion ZnO Co-Doped (Er, Yb) Nanopowders Synthesized via the Sol-Gel Process for Photovoltaic Applications. Mater (Basel) 2022, 15 (21), 7828.
55. Ashraf H, Meer B, Iqbal J, Ali JS, Andleeb A, Butt H, Zia M, Mehmood A, Nadeem M, Drouet S, et al. Comparative evaluation of chemically and green synthesized zinc oxide nanoparticles: their in vitro antioxidant, antimicrobial, cytotoxic and anticancer potential towards HepG2 cell line. J Nanostructure Chem. 2022;13:243–61.
56. Safwat G, Soliman ESM, Mohamed HRH. Induction of ROS mediated genomic instability, apoptosis and G0/G1 cell cycle arrest by erbium oxide nanoparticles in human hepatic Hep-G2 cancer cells. Sci Rep. 2022;12:16333.
57. Dewey MJ, Timmer KB, Blystone A, Lu C, Harley BAC. Evaluating osteogenic effects associated with the incorporation of ascorbic acid in mineralized collagen scaffolds. J Biomed Mater Res A. 2024;112:336–47.
58. Ali A, Riaz S, Khalid W, Fatima M, Mubeen U, Babar Q, Manzoor MF, Zubair Khalid M, Madilo FK. Potential of ascorbic acid in human health against different diseases: an updated narrative review. Int J Food Prop. 2024;27:493–515.
59. Prasad A, Rathi D, Sedlarova M, Manoharan RR, Prudkova E, Pospisil P. Differential effects of ascorbic acid on monocytic cell morphology and protein modification: Shifting from pro-oxidative to antioxidant properties. Biochem Biophys Rep. 2024;37:101622.
60. Maity J, Pal P, Pal R, Mukhopadhyay PK. Co-administration of L-Ascorbic Acid and alpha-Tocopherol Alleviates Arsenic-Induced Immunotoxicities in the Thymus and Spleen by Dwindling Oxidative Stress-Induced Inflammation. Biol Trace Elem Res. 2024;202:2199–227.
61. Mishra G, Awasthi R, Mishra SK, Singh AK, Tiwari AK, Singh SK, Nandi MK. Development of Epigallocatechin and Ascorbic Acid Dual Delivery Transferosomes for Managing Alzheimer's Disease: In Vitro and in Vivo Studies. ACS Omega. 2024;9:35463–74.
62. Seyama Y, Sudo K, Yamada T, Tsuchiya K, Nakamura Y. Ascorbic acid predominantly kills cancer stem cell-like cells in the hepatocellular carcinoma cell line Li-7 and is more effective at low cell density and in small spheroids. Biochem Biophys Res Commun. 2024;709:149816.
63. Dong W, Peng Y, Chen G, Xie Z, Xu W, Zhou W, Mi J, Lu L, Sun Y, Zeng X, et al. 2-O-β-D-Glucopyranosyl-L-ascorbic acid, an ascorbic acid derivative isolated from the fruits of Lycium barbarum L., ameliorates high fructose-induced neuroinfl ammation in mice: involvement of gut microbiota and leaky gut. Food Sci Hum Wellness. 2024;13:241–53.

64. Saleemi MA, Alallam B, Yong YK, Lim V. Synthesis of Zinc Oxide Nanoparticles with Bioflavonoid Rutin: Characterisation, Antioxidant and Antimicrobial Activities and In Vivo Cytotoxic Effects on Artemia Nauplii. Antioxid (Basel) 2022, 11 (10), 1853.
65. Li R, Zhao Y, Zhang T, Ju Z, Ji X, Cui Y, Wang L, Xiao H. Pd nanoparticles stabilized by bitter gourd polysaccharide with peroxidase properties for H(2)O(2) detection. Int J Biol Macromol. 2023;233:123513.
66. Wang L, Shi J, Wang P, Rong R. High-sensitive detection of H2O2 in biological systems by persistent luminescent nanoprobes. Chem Eng J 2024, 486, 150291.
67. Mohiuddin AK, Jeon S. Highly efficient Ag doped delta-MnO(2) decorated graphene: Comparison and application in electrochemical detection of H(2)O(2). Appl Surf Sci. 2022;592:153162.
68. Ramzan I, Bashir M, Saeed A, Khan BS, Shaik MR, Khan M, Shaik B, Khan M. Evaluation of Photocatalytic, Antioxidant, and Antibacterial Efficacy of Almond Oil Capped Zinc Oxide Nanoparticles. Mater (Basel) 2023, 16 (14), 5011.
69. Valgimigli L, Baschieri A, Amorati R. Antioxidant activity of nanomaterials. J Mater Chem B. 2018, 6, 2036.

Publisher's note